Available online at www.sciencedirect.com
ScienceDirect
Journal of Computational Physics 227 (2007) 1306–1339
JOURNAL OF COMPUTATIONAL PHYSICS
www.elsevier.com/locate/jcp

A new family of high-order compact upwind difference schemes with good spectral resolution

Qiang Zhou, Zhaohui Yao, Feng He *, M.Y. Shen

Department of Engineering Mechanics, Tsinghua University, Beijing 100084, People's Republic of China

Received 22 December 2006; received in revised form 3 September 2007; accepted 4 September 2007
Available online 20 September 2007

Abstract

This paper presents a new family of high-order compact upwind difference schemes. Unknowns included in the proposed schemes are not only the values of the function but also those of its first and higher derivatives. Derivative terms in the schemes appear only on the upwind side of the stencil. One can calculate all the first derivatives exactly as one solves explicit schemes when the boundary conditions of the problem are non-periodic. When the proposed schemes are applied to periodic problems, only periodic bi-diagonal matrix inversions or periodic block-bi-diagonal matrix inversions are required. Resolution optimization is used to enhance the spectral representation of the first derivative, and this produces a scheme with the highest spectral accuracy among all known compact schemes. For non-periodic boundary conditions, boundary schemes constructed in virtue of the assistant scheme make the schemes not only possess stability for any selective length scale on every point in the computational domain but also satisfy the principle of optimal resolution. Also, an improved shock-capturing method is developed. Finally, both the effectiveness of the new hybrid method and the accuracy of the proposed schemes are verified by executing four benchmark test cases.

Keywords: Compact upwind difference scheme; Optimized resolution; Hybrid scheme; Boundary closure; Shock-capturing; High-order scheme; Spectral analysis; Full spatial stability

1. Introduction

Compact high-order finite difference schemes have been extensively studied and widely used to compute problems involving incompressible, compressible and hypersonic flows [13–22,39], computational aeroacoustics [23–27,36,48], computational electromagnetics [28–30] and several other practical applications [31–35]. Using compact stencils that relate various derivatives with function values at discrete nodes, compact schemes not only offer higher order approximations to differential operators but provide higher resolution characteristics for the same number of scheme points in comparison to explicit finite difference schemes. Due to their high formal order, good spectral resolution and their flexibility, compact high-order finite

* Corresponding author. Tel.: +86 10 62787470; fax: +86 10 62782639.
E-mail address: hefeng@tsinghua.edu.cn (F. He).

0021-9991/$ - see front matter
doi:10.1016/j.jcp.2007.09.008

difference schemes are the most attractive schemes for flows with multiscales, e.g., turbulence. The smallest scales, which are dictated by the physical viscosity of the flow, become unresolvable with the mesh size, and they suffer from instabilities. There are three remedies [1] for this unwanted behavior: explicit filtering, artificial viscosity and schemes with inherent dissipation. Of these three remedies, the satisfactory way of physically dissipating unresolvable wavenumbers is to use a high-order compact upwind scheme. Upwinding in compact schemes has earlier been incorporated by Tolstykh [2,3] through a Murman-type switch [4]. The CUD-3 and CUD-5 [5] were their most famous schemes. In subsequent years, Tolstykh constructed compact upwind schemes with arbitrary order via linear combinations of "elementary" CUD operators of fixed order (say, third order). Some details of the technique (multioperator) can be found, for example, in [6,7]. However, in their work, no effort was made to optimize the resolution characteristics. An optimized version using a free parameter was introduced by Adams and Shariff [40]. Not adopting the idea of "multioperator", which was interesting but a bit complicated, Adams and Shariff [40] constructed their schemes basically following Lele's technique [12], namely, based on Hermite interpolation, but dropped the requirement of symmetric/antisymmetric coefficients. In this paper, the method of developing compact upwind schemes is almost the same as Adams and Shariff's [40] except that the second derivative appears. We also note that some particular forms of compact upwind schemes have been proposed in [8–10]. Lele [12] emphasized the distinction between the order of approximation and the spectral resolution and applied Pade schemes for the solution of compressible and incompressible flow problems. Mahesh [37] presented and analyzed combined compact uniform grid finite difference schemes (C-D schemes) which evaluate the first and the second derivative simultaneously. The generalized compact (GC) schemes and some of their important properties were discussed by Shen et al. [11]. The GC schemes can be considered as a more general version of the standard Pade schemes discussed by Lele [12]. The appearance of higher derivatives in both C-D schemes and GC schemes gives rise to the spectral accuracy of the first derivative. The family of compact upwind schemes developed in this study can be categorized as GC schemes. They have a speed advantage as well as higher resolution in comparison to other compact schemes. Often, the tri-diagonal matrix inversion is required in applications of the commonly used compact schemes. However, using the proposed schemes, one can sequentially calculate all the derivatives by explicit means if the boundary value problem is solved. When our schemes are applied to periodic problems, only periodic bi-diagonal matrix inversions or periodic block-bi-diagonal matrix inversions are required.

Sengupta et al. [36] pointed out that the definition of G–K–S stability [38] (also known as Lax stability) might be too weak and hence it would not be a practical option to use those compact schemes for DNS, CAA and CEM, which are only G–K–S stable. They also developed a Fourier–Laplace transform based spectral method for the purpose of evaluating the spectral resolution, numerical stability and dispersion relation preservation (DRP) property of any discrete computing technique. Using this analysis, some well-known compact schemes that were found to be G–K–S and time stable are shown to be unstable for selective length scales [36]. Subsequently, further improvements of this analysis method were obtained in [49–51] to provide results for different spatial and temporal discretization methods. In the following sections, we refer to these schemes as full spatial stable (referred to later on in this paper as FS-stable for short) if they are stable for all interior and boundary points analyzed in isolation by this method. We consider the linear wave equation

$$\frac{\partial u}{\partial t}+\frac{\partial u}{\partial x}=0 \tag{1.1}$$

as a model equation, working in the computational plane with a uniform grid of size h and total point number N. It is assumed that computations with nonuniform grids can define analytical mappings between the nonuniform grid and a corresponding uniform grid. The metrics of the mapping may then be used to relate the derivatives on the uniform grid to those on the nonuniform grid. If the Dirichlet boundary condition is adopted on the first point, the FS-stability means that spatial discretization schemes are all stable for points $j=2,3,\ldots,N$. In the present paper, our consideration is confined to this situation. In order to achieve FS-stability, a new method for constructing stable boundary schemes is developed. Numerical examples show that schemes that possess the property of FS-stability are asymptotically stable both in the scalar and system case.

If the flow fields involve shock waves, schemes should also be essentially oscillation-free near the discontinuities. In recent years, many efforts have been devoted to the development of high resolution shock-capturing

schemes that are higher-order accurate in smooth regions. For details of the background on this issue the reader is referred to [39]. Also, it is pertinent to pay attention to the commonly used Jameson–Schmidt–Turkel switching function (JST switch) [46], which can be interpreted as a limiter. The switch activates the dissipation term (usually the second-difference term) at not only discontinuities but also extrema in the smooth region, which may be too dissipative for DNS and other high-resolution calculations. A novel switch based on second derivatives was introduced by Sengupta et al. [50]. The method was very simple and was proven to be effective for diagnosing the discontinuity for the Burgers equation. However, the threshold value must be selected cautiously, because it depends on what problem is being solved.

Ren et al. [39] considers the hybrid scheme as the weighted average of two sub-schemes: the conservative compact scheme proposed by Pirozzoli [45] and the WENO scheme. The weight function is designed to be continuous so that the abrupt transition from one sub-scheme to another is avoided. The shortcoming of the smoothness indicator in Ref. [39] is that it may take some points in smooth waves, especially in high-wavenumber waves, as points of discontinuity. In order to eliminate this deficiency, we identify the discontinuity in two steps, which are discussed in detail in Section 4.1. Numerical tests show a significant improvement in resolution for scalar cases and flows with complex structures.

This paper is structured in the following manner. In the next section, we derive a new family of compact upwind schemes in which free parameters are optimized for higher spectral resolution. Also, the dispersive and dissipative features of our schemes are compared to other compact schemes. In Section 3, a new method for constructing boundary schemes is presented. In order to pursue good resolution, the boundary schemes are optimized. The third section also illustrate the process of solving derivatives when our schemes are adopted with periodic boundaries. In Section 4, the schemes are made shock-capturing by hybridizing them with WENO schemes. The hybridization procedure basically follows Ren et al.'s [39] method. An important improvement is achieved by filtering out points in smooth waves that might be mistaken for points of discontinuity, which, though important, has not attracted much attention before. In Section 5, the computational cost of the first derivatives is assessed. In Section 6, four benchmark test cases are executed to confirm the effectiveness of the hybrid schemes when applied to systems of equations. The concluding remarks are given in Section 7.

2. The interior scheme

2.1. The interior schemes and resolution optimization

Consider the following model equation and its semi-discrete approximation

$$\frac{\partial u}{\partial t} + c\frac{\partial u}{\partial x} = 0, \quad c \text{ is a positive constant,} \tag{2.1}$$

$$\frac{\partial u}{\partial t} + cF_j = 0, \tag{2.2}$$

where F_j is an approximation of the first derivative $\partial u/\partial x$, and F_j can be obtained from the spatial discretization scheme. In the present paper, we are concerned with the GC schemes [11] from which F_j can be derived. A simple example of GC schemes is given in the following expressions:

$$h(a_{1,-1}F_{j-1} + a_{1,0}F_j + a_{1,1}F_{j+1}) + h^2(a_{2,-1}S_{j-1} + a_{2,0}S_j + a_{2,1}S_{j+1}) = \sum_{n=-k_1}^{k_2} a_{0,n}u_{j+n}, \tag{2.3a}$$

$$h(\bar{a}_{1,-1}F_{j-1} + \bar{a}_{1,0}F_j + \bar{a}_{1,1}F_{j+1}) + h^2(\bar{a}_{2,-1}S_{j-1} + \bar{a}_{2,0}S_j + \bar{a}_{2,1}S_{j+1}) = \sum_{n=-k_1}^{k_2} \bar{a}_{0,n}u_{j+n}, \tag{2.3b}$$

where S_j is the approximation of $\partial^2 u/\partial x^2$. $a_{1,i}$, $a_{2,i}$, $\bar{a}_{1,i}$, $\bar{a}_{2,i}$ $(i = -1, 0, 1)$ and $a_{0,n}$, $\bar{a}_{0,n}$ $(n = -k_1, \ldots, k_2)$ are coefficients to be determined. Let $a_{1,1} = \bar{a}_{1,1} = a_{2,1} = \bar{a}_{2,1} = 0$; then we obtain the following expected form in which derivative terms are confined to the left side of the stencil:

$$h(a_{1,-1}F_{j-1}+a_{1,0}F_j)+h^2(a_{2,-1}S_{j-1}+a_{2,0}S_j)=\sum_{n=-k_1}^{k_2}a_{0,n}u_{j+n}, \tag{2.4a}$$

$$h(\bar{a}_{1,-1}F_{j-1}+\bar{a}_{1,0}F_j)+h^2(\bar{a}_{2,-1}S_{j-1}+\bar{a}_{2,0}S_j)=\sum_{n=-k_1}^{k_2}\bar{a}_{0,n}u_{j+n}. \tag{2.4b}$$

In this family of compact schemes, one or two coefficients are defined as free parameters for resolution optimization. The method of optimizing the resolution is almost the same as the one used in the literature by Adams and Shariff [40]. The details of determining coefficients are shown below.

First, a three-point third-order (2.4)-like scheme is developed. We set $m=2,k_1=1,k_2=1$, where m denotes the highest order of the derivatives that appear in the schemes, and $j-k_1$ and $j+k_2$ are the smallest and largest node serial numbers in the stencil, respectively. Substituting the set values of k_1 and k_2 into Eq. (2.4a), we have

$$h(a_{1,-1}F_{j-1}+a_{1,0}F_j)+h^2(a_{2,-1}S_{j-1}+a_{2,0}S_j)=\sum_{n=-1}^{1}a_{0,n}u_{j+n}. \tag{2.5}$$

There are seven coefficients in this scheme, one of which disappears due to normalization. The constraint of the order conditions (equality up to a term of order $O(h^3)$ in Eq. (2.5) requires four equations based on the Taylor expansion.) leaves only two free parameters. The other coefficients are linear functions of the two free parameters.

Set $a_{1,0}=1$ for normalization, and let $a_{0,0}$, $a_{2,0}$ be the two free parameters. Then we get two linearly independent equations by substituting $a_{0,0}=a$, $a_{2,0}=0$ and $a_{0,0}=0$, $a_{2,0}=b$ into Eq. (2.5), respectively. The scheme is the combination of the following two equations:

$$h(a_{1,-1}F_{j-1}+F_j)+h^2(a_{2,-1}S_{j-1})=a_{0,-1}u_{j-1}+au_j+a_{0,1}u_{j+1}, \tag{2.6a}$$

$$h(\bar{a}_{1,-1}F_{j-1}+F_j)+h^2(\bar{a}_{2,-1}S_{j-1}+bS_j)=\bar{a}_{0,-1}u_{j-1}+\bar{a}_{0,1}u_{j+1}, \tag{2.6b}$$

where

$$a_{1,-1}=3a/4-1/4,\quad a_{0,-1}=-7a/8-3/8,\quad a_{2,-1}=a/4-1/4,\quad a_{0,1}=-a/8+3/8,$$
$$\bar{a}_{0,-1}=-3/8-3b/4,\quad \bar{a}_{2,-1}=-1/4+b/2,\quad \bar{a}_{0,1}=3/8+3b/4,\quad \bar{a}_{1,-1}=-1/4+3b/2.$$

The dispersion and dissipation errors of Eqs. (2.6a) and (2.6b) are analyzed in the wavenumber domain. Fourier analysis provides an effective way to quantify these errors of difference schemes. The Fourier transforms of the left and right sides of Eqs. (2.6a) and (2.6b) can be

$$\mathrm{i}\bar{\kappa}(a_{1,-1}\mathrm{e}^{-\mathrm{i}\kappa}+1)\tilde{u}-\bar{\bar{\kappa}}^2a_{2,-1}\tilde{u}=(a_{0,-1}\mathrm{e}^{-\mathrm{i}\kappa}+a+a_{0,1}\mathrm{e}^{\mathrm{i}\kappa})\tilde{u}, \tag{2.7a}$$

$$\mathrm{i}\bar{\kappa}(\bar{a}_{1,-1}\mathrm{e}^{-\mathrm{i}\kappa}+1)\tilde{u}-\bar{\bar{\kappa}}^2(\bar{a}_{2,-1}\mathrm{e}^{-\mathrm{i}\kappa}+b)\tilde{u}=(\bar{a}_{0,-1}\mathrm{e}^{-\mathrm{i}\kappa}+\bar{a}_{0,1}\mathrm{e}^{\mathrm{i}\kappa})\tilde{u}. \tag{2.7b}$$

In Eqs. (2.7), $\mathrm{i}=\sqrt{-1}$; and κ is called the scaled wavenumber because it is the product of wavenumber k and grid size h; $\bar{\kappa}$ and $\bar{\bar{\kappa}}^2$ are functions of κ and are called the modified scaled wavenumber for the first and second derivative operators, respectively. The differences between $\bar{\kappa}$ and κ and between $\bar{\bar{\kappa}}^2$ and κ^2 represent the differencing error in the wavenumber domain. $\bar{\kappa}$ can be derived from (2.7a) and (2.7b) after simple diminution operation, so it is a function of a, b and κ, namely $\bar{\kappa}=\bar{\kappa}(a,b,\kappa)$. $\bar{\kappa}$ can be divided into real and imaginary parts, which represent the dispersion and the dissipation error, respectively. To ensure that the scheme is a good approximation of the first derivative, the modified scaled wavenumber should agree with the corresponding scaled wavenumber in as wide a range of wavenumbers as possible. We optimize the scheme numerically by minimizing a target function, which is

$$\varepsilon=\alpha\int_0^{top}(\kappa-\mathrm{Re}(\bar{\kappa}))^2\,\mathrm{d}\kappa+\beta\int_0^{top}(\mathrm{Im}(\bar{\kappa}))^2\,\mathrm{d}\kappa. \tag{2.8}$$

Free parameters a and b enter the definition of ε through the substitution of the expression of $\bar{\kappa}$ into Eq. (2.8). The upper limit of integration in Eq. (2.8) is chosen as $top\leqslant\pi$. α is the weight for the dispersion error; β is the weight for the dissipation error. We require the scheme to satisfy two constraints:

(a) The scheme is required to satisfy the necessary stability criterion [40] (Note that c is positive in Eq. (2.1).)

$$-\mathrm{Im}(\bar{\kappa}) \geqslant 0; \tag{2.9}$$

(b) Solving Eqs. (2.6a) and (2.6b), F_j and S_j can be expressed as linear functions of F_{j-1} and S_{j-1} as follows:

$$F_j = \tilde{a}_{1,-1}F_{j-1} + \tilde{a}_{2,-1}S_{j-1} + \sum_{n=-1}^{1} \tilde{a}_{0,n}u_{j+n}, \tag{2.10a}$$

$$S_j = \tilde{\tilde{a}}_{1,-1}F_{j-1} + \tilde{\tilde{a}}_{2,-1}S_{j-1} + \sum_{n=-1}^{1} \tilde{\tilde{a}}_{0,n}u_{j+n}. \tag{2.10b}$$

In order not to magnify the numerical error in F_j and S_j which is due to the round-off error of the machine or other reasons, the following constraints must be added:

$$|\tilde{a}_{1,-1}| + |\tilde{a}_{2,-1}| < 1,$$
$$|\tilde{\tilde{a}}_{1,-1}| + |\tilde{\tilde{a}}_{2,-1}| < 1,$$

where $\tilde{a}_{1,-1}, \tilde{a}_{2,-1}, \tilde{\tilde{a}}_{1,-1}$ and $\tilde{\tilde{a}}_{2,-1}$ are functions of h and coefficients in Eqs. (2.6). Here we set $h = 1$ for simplicity.

Locally optimal free coefficients that minimize ε under the constraints (a) and (b) are obtained numerically. A standard sequential quadratic programming (SQP) method [59] is used. The selection of this algorithm is based on its ready availability (as the IMSL routine NCONF) and on its superior performance and reliability compared to other approaches [59]. For details the reader is referred to [59,60]. The optimization result strongly depends on the particular choice of parameters in Eq. (2.8) and is also sensitive to the initial guess.

In order to achieve high resolution, we set $\alpha = 1$ and $\beta = 0$ in the optimization of the scheme. Choosing $top = 1.5$, we find the optimal parameters are $a = 0.9033682206946493$ and $b = 0.3268142702664771$. So far the three-point third-order optimized GC scheme has been developed. We call this scheme 3P3Om2 for briefness in this paper, where the three numbers in the name sequentially denote the number of points included, the order of the formal accuracy and the highest order of the derivatives appearing in the scheme, respectively.

We can construct schemes of this family with up to seventh-order accuracy in the same way. All of these schemes have high resolution and the dissipation properties are also satisfying.

Another third-order accuracy scheme is

$$a_{1,-1}F_{j-1} + a_{1,0}F_j = (a_{0,-1}u_{j-1} + au_j + a_{0,1}u_{j+1} + a_{0,2}u_{j+2})/h, \tag{2.11}$$

which provides an a-family of third-order schemes with

$$a_{1,0} = 1, \quad a_{0,1} = -a/2 + 3/4, \quad a_{1,-1} = a/3 + 1/6, \quad a_{0,-1} = -11a/18 - 23/36, \quad a_{0,2} = a/9 - 1/9.$$

$a = 0.8915319975352406$ gives the optimal resolution for the first derivative. For briefness, this scheme will be referred to as the 4P3O m1 scheme later.

The seventh-order accuracy scheme is

$$h(a_{1,-1}F_{j-1} + a_{1,0}F_j) + h^2(a_{2,-1}S_{j-1} + a_{2,0}S_j) = \sum_{n=-1}^{5} a_{0,n}u_{j+n}, \tag{2.12a}$$

$$h(\bar{a}_{1,-1}F_{j-1} + \bar{a}_{1,0}F_j) + h^2(\bar{a}_{2,-1}S_{j-1} + \bar{a}_{2,0}S_j) = \sum_{n=-1}^{5} \bar{a}_{0,n}u_{j+n}. \tag{2.12b}$$

The free parameters chosen for optimization in the seventh-order accuracy scheme are coefficients of S_j and u_j. Letting $a_{2,0} = 0$, $a_{0,0} = a$, $\bar{a}_{2,0} = b$ and $\bar{a}_{0,0} = 0$, we express other coefficients in the following expressions:

$$a_{2,-1} = a/12 + 17/720, \quad a_{1,-1} = 49a/120 + 2033/7200, \quad a_{1,0} = 1,$$
$$a_{0,-1} = -13489a/21600 - 974513/1296000, \quad a_{0,1} = -5a/8 + 103/96, \quad a_{0,2} = 10a/27 - 73/162,$$
$$a_{0,3} = -5a/32 + 21/128, \quad a_{0,4} = a/25 - 29/750, \quad a_{0,5} = 11/2592 - a/216,$$

$$\bar{a}_{2,-1} = 203b/720 + 17/720, \quad \bar{a}_{1,-1} = 763b/800 + 2033/7200, \quad \bar{a}_{1,0} = 1,$$
$$\bar{a}_{0,-1} = -393587b/1296000 - 974513/1296000, \quad \bar{a}_{0,1} = -31b/96 + 103/96, \quad \bar{a}_{0,2} = 82b/81 - 73/162,$$
$$\bar{a}_{0,3} = -65b/128 + 21/128, \quad \bar{a}_{0,4} = -29/750 + 52b/375, \quad \bar{a}_{0,5} = 11/2592 - 43b/2592.$$

Choosing $top = 2.5$, we find the optimal parameters are $a = 0.8339762325591169$ and $b = 0.6167415381304258$. Later on in the present paper, this seventh-order accuracy scheme is referred to as the 7P7Om2 scheme.

For values of coefficients of the three schemes proposed above, the reader is referred to Appendix A.

Following the manner mentioned above, we also constructed 4P4Om2, 5P5Om2 and 6P6Om2 schemes. Though their computational costs are almost the same as that of the 7P7Om2 scheme, their spectral resolution is not as good as that of the 7P7Om2 scheme. Therefore, they are not listed here.

2.2. Evaluation of the first derivative

The real part of the modified scaled wavenumbers for the first derivative is shown in Fig. 1. The 3P3Om2 scheme, which is almost the same as the 4P3Om1 scheme, seems to follow the exact solution more closely than the standard sixth-order Pade scheme, though it has a narrower stencil width. The 7P7Om2 scheme has the same stencil width as the tenth-order Pade scheme; however, it is seen to have much higher spectral accuracy than the tenth-order Pade scheme. As a matter of fact, the proposed 7P7Om2 scheme is the most accurate one in the spectral plane among all known compact schemes. The CUD-5 scheme, which has been extensively used for solving various compressible and incompressible flows described by the Navier–Stokes equations [61–63], however, has relatively poor spectral accuracy. So the proposed schemes are attractive alternatives to the CUD-5 scheme. Table 1 provides a more quantitative comparison of the resolution properties of the schemes, in which we compare these schemes using the function $\tilde{\varepsilon} = \int_0^{top} (\kappa - \mathrm{Re}(\bar{\kappa}))^2 \, \mathrm{d}\kappa$. Obviously, when the *top* stays the same, the resolution increases with the decrease of $\tilde{\varepsilon}$.

Fig. 2 shows that 4P3Om1, 3P3Om2 and 7P7Om2 have built-in numerical viscosity at high wavenumbers. It can be seen that the 7P7Om2 scheme is less dissipative at moderate wavenumbers than the CUD-5 scheme, which means that the smaller scales can be better resolved by the 7P7Om2 scheme when they are used to solve problems with multi-scales, e.g., turbulence. All the upwind compact schemes shown here have strong dissipation at high wavenumbers. The dissipation can be useful to suppress non-resolved small-scale instabilities. It can also be helpful to inhibit odd-even decoupling observed in DNS with symmetric compact schemes [56]. However, Pade schemes and the C-D scheme are symmetric and essentially non-dissipative. When they are

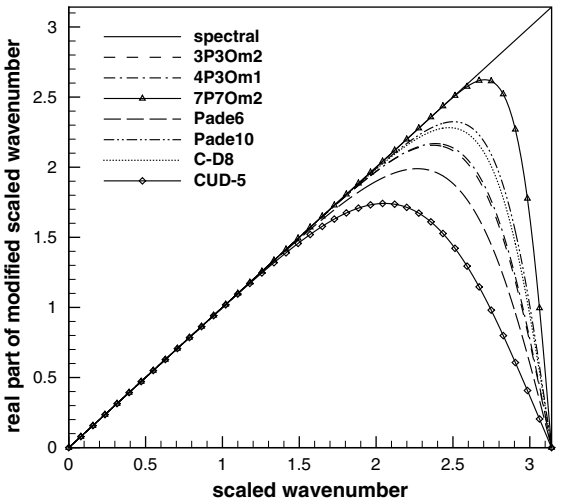

Fig. 1. Plot of real part of modified scaled wavenumber vs. scaled wavenumber for first derivative approximations. The CUD-5 scheme here is the $L_5^{(1)}$ version with $s = 1.5$ (see Ref. [5]).

Table 1
Comparison of the resolving efficiency

	$top = 1.5$	$top = 1.7$	$top = 2.0$
3P3Om2	0.508557E−08	0.596528E−06	0.706533E−04
4P3Om1	0.242689E−07	0.109257E−05	0.766258E−04
7P7Om2	0.441636E−07	0.104085E−06	0.131466E−06
Sixth-Pade	0.107860E−04	0.815729E−04	0.120426E−02
Tenth-Pade	0.358530E−08	0.838330E−07	0.573833E−05
Eighth-order C-D	0.204677E−07	0.343684E−06	0.158558E−04
CUD-5	0.137679E−03	0.883426E−03	0.952471E−02

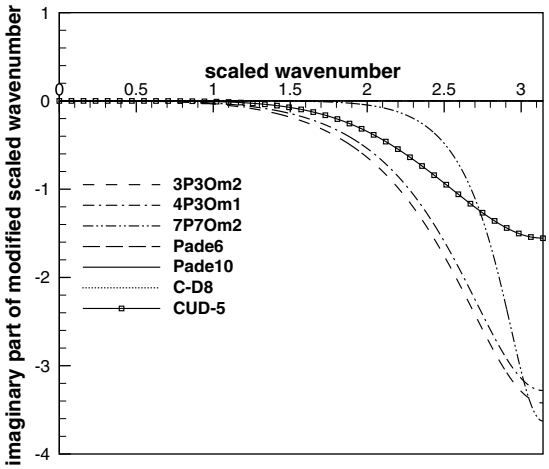

Fig. 2. Plot of imaginary part of modified scaled wavenumber vs. scaled wavenumber for first derivative approximations.

used in turbulence simulations, extra stabilizing filters are required, which are equivalent to adding numerical dissipation in an ad hoc manner, to suppress poorly resolved waves.

2.3. Evaluation of the second derivative

There are second derivatives in the formulae of the 3P3Om2 and 7P7Om2 schemes that may have further use [37], as for the diffusion terms in Navier–Stokes equations. Because of this, even though they are not our main concern, the properties of the second derivatives should also be assessed. The plot of the real part of modified scaled wavenumber for the second derivative against scaled wavenumber for a variety of schemes is presented in Fig. 3. Generally speaking [57], it is better to obtain approximations of the second derivatives directly rather than indirectly (i.e., applying the first derivative twice). This statement can be verified by comparing the curves of the Pade6 and Pade10 schemes for the second derivative with those using the corresponding first derivatives twice. However, it seems that our case is the opposite situation. The second derivatives obtained directly from 3P3Om2 and 7P7Om2 schemes, are accurate only with lower wavenumbers, which are only comparable with the results of the explicit eighth scheme with first derivatives used twice. However, the results when the first derivatives are used twice in the 4P3Om1, 3P3Om2 and 7P7Om2 schemes are a bit better, especially in the 7P7Om2 case, which achieves high spectral accuracy to about 4/5 of the Nyquist wavenumber. This situation can be attributed to our main motivation, which is to develop and optimize schemes for good spectral accuracy for the first derivative. At first, we did not consider what kind of influence the optimization would have on the second derivative, but later we learned that the influence was negative; in other words, good resolution was achieved at the sacrifice of the second derivative. As a whole, for the direct case, the second derivatives from 3P3Om2 and 7P7Om2 show no competition with those from other compact schemes. For the indirect case, only 4P3Om1 is comparable with other schemes, and the 3P3Om2 and

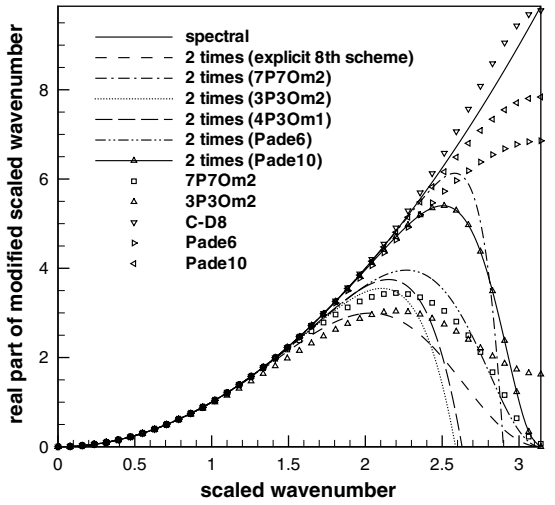

Fig. 3. Plot of real part of modified scaled wavenumber vs. scaled wavenumber for second derivative approximations. The "2 times" in the figure denotes the first derivative scheme was used two times.

7P7Om2 schemes are too time-consuming to be adopted in practice. Based on the above analysis, we do not recommend 3P3Om2 or 7P7Om2 for the calculation of second derivatives through either the direct or indirect methods. The 4P3Om1 scheme may be an alternative to other schemes for some problems because of its speed advantage (see Section 5).

The plot of the imaginary part of the modified scaled wavenumber for the second derivative against the scaled wavenumber for the proposed schemes is presented in Fig. 4. It illustrates the dispersion property of the second derivative. All symmetric schemes for the second derivative have no dispersion error, which is why they do not appear in the plot. However, upwind schemes have obvious deviation from the zero line at high wavenumbers. The dispersion errors of the second derivatives computed directly from 3P3Om2 and 7P7Om2 are a bit bigger than that computed indirectly by 7P7Om2, which is better in the sense that there is essentially no error at a wider range of wavenumbers. The worst results in these schemes come from indirect calculation with the 3P3Om2 and 4P3Om1 schemes.

Based on the above analysis, a conclusion can be reached that upwind schemes do not perform very well if used for second derivatives. So, for the viscous terms in N–S equations, commonly used symmetric schemes are more recommended.

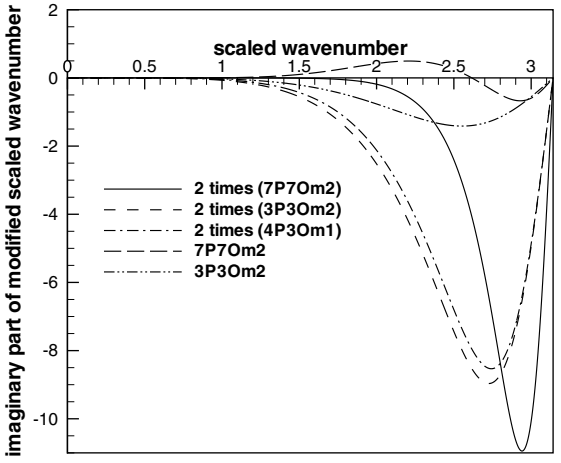

Fig. 4. Plot of imaginary part of modified scaled wavenumber vs. scaled wavenumber for second derivative approximations. The "2 times" in the figure denotes the first derivative scheme was used two times.

2.4. Solution strategies with periodic boundary conditions

We consider a uniform 1-D mesh with the grid space denoted by h, consisting of N points: $x_1, x_2, \ldots, x_{j-1}, x_j, x_{j+1}, \ldots, x_N$. In order to illustrate the solution strategies with periodic boundary conditions, for simplicity and no loss of generality, we take the 4P3Om1 scheme for example and implement it on all points. Therefore we have (for convenience, in the following expressions in this subsection, we let A stand for $a_{1,-1}$, B stand for $a_{1,0}$, U_j for the first derivative of the function u on point j, and D_j for $(a_{0,-1}u_{j-1} + au_j + a_{0,1}u_{j+1} + a_{0,2}u_{j+2})/h$):

$$\begin{bmatrix} B & & & & & & A \\ A & B & & & & & \\ & A & B & & & & \\ & & \ddots & \ddots & & & \\ & & & A & B & & \\ & & & & A & B & \end{bmatrix} \begin{bmatrix} U'_1 \\ U'_2 \\ U'_3 \\ \vdots \\ U'_{n-1} \\ U'_n \end{bmatrix} = \begin{bmatrix} D_1 \\ D_2 \\ D_3 \\ \vdots \\ D_{n-1} \\ D_n \end{bmatrix}. \tag{2.13}$$

Provided $B \neq 0$, the operations corresponding to $\left(-\left(\frac{A}{B}\right)E_j + E_1\right) \to E_1$ (E_j stands for the jth row of the system (2.13)) are performed for each $j = n, n-1, \ldots 2$ to eliminate the element A in the first row. The resulting system has the form

$$\begin{bmatrix} B + A(-\frac{A}{B})^{n-1} & & & & & & \\ & A & & B & & & \\ & & & A & B & & \\ & & & & \ddots & \ddots & \\ & & & & & A & B \\ & & & & & & A & B \end{bmatrix} \begin{bmatrix} U'_1 \\ U'_2 \\ U'_3 \\ \vdots \\ U'_{n-1} \\ U'_n \end{bmatrix}$$
$$= \begin{bmatrix} D_1 + \left(-\frac{A}{B}\right)D_n + \left(-\frac{A}{B}\right)^2 D_{n-1} + \cdots \left(-\frac{A}{B}\right)^{m+1} D_{n-m} + \cdots + \left(-\frac{A}{B}\right)^{n-1} D_2 \\ D_2 \\ D_3 \\ \vdots \\ D_{n-1} \\ D_n \end{bmatrix}. \tag{2.14}$$

Then forward substitution can be performed for the solution. Normally, there is no need to do the elimination work from n to 2. The ratio A/B is less than 1 for numerical stability, so if n is bigger than some value n_0 we will have $(-A/B)^{n-1} < 1.0\text{E}{-}16$ (n_0 is the minimum positive integer satisfying this inequality), which is comparable to the round-off error of the machine. The fact illustrated above means that there is no influence on the result of the computation if the (2.15)-like system with $n > n_0$ is solved.

$$\begin{bmatrix} B & & & & & \\ A & B & & & & \\ & A & B & & & \\ & & \ddots & \ddots & & \\ & & & A & B & \\ & & & & A & B \end{bmatrix} \begin{bmatrix} U'_1 \\ U'_2 \\ U'_3 \\ \vdots \\ U'_{n-1} \\ U'_n \end{bmatrix} = \begin{bmatrix} D_1 + \left(-\frac{A}{B}\right)D_n + \left(-\frac{A}{B}\right)^2 D_{n-1} + \cdots \left(-\frac{A}{B}\right)^{n_0-1} D_{n-n_0+2} \\ D_2 \\ D_3 \\ \vdots \\ D_{n-1} \\ D_n \end{bmatrix}. \tag{2.15}$$

So far we have learned that the solving of the system (2.13) is very efficient. When n is adequately large, it is comparable with the solving of the system with non-periodic conditions. If the 7P7Om2 or 3P3Om2 scheme is adopted, the resulting system can be solved in the same way except that A, B are 2×2 matrices and U_j, D_j are vectors of two elements.

3. Boundary closures

3.1. Boundary treatment for full spatial stability

A von Neumann matrix spectral analysis was developed in Ref. [36] to analyze spatial discretization schemes for any explicit or implicit scheme to investigate the full domain simultaneously. This analysis allows one to evaluate various boundary closures and their effects on the domain interior. Using this analysis, Sengupta et al. [36] found that some well-known compact schemes that were found to be G–K–S and time stable are unstable for selective length scales, which is attributed to boundary closure. In this paper, we suggest a new boundary treatment based on the interior schemes to remove this drawback.

All compact schemes can be written in an equivalent explicit form:

$$u' = Cu, \tag{3.1}$$

where $u = [\ldots u_{j-1}, u_j, u_{j+1}, \ldots]^{\mathrm{T}}$ and $u' = [\ldots u'_{j-1}, u'_j, u'_{j+1}, \ldots]^{\mathrm{T}}$. The analysis [36,47,58] is performed in the wavenumber plane, with the unknown expressed in terms of the bi-lateral Laplace transform pair:

$$u(x_j) = \int U(k) \mathrm{e}^{\mathrm{i}kx_j}\, \mathrm{d}k. \tag{3.2}$$

The derivative of the function at x_j can be expressed for the Fourier spectral method as

$$u'(x_j) = \int \mathrm{i}kU(k) \mathrm{e}^{\mathrm{i}kx_j}\, \mathrm{d}k, \tag{3.3}$$

and the corresponding expression for the numerical derivative using other discrete computing methods can be written as

$$u'(x_j) = \int \mathrm{i}k_{\mathrm{eq}}U(k) \mathrm{e}^{\mathrm{i}kx_j}\, \mathrm{d}k. \tag{3.4}$$

Using Eq. (3.2) in Eq. (3.1) and comparing with Eq. (3.4), it can be readily shown that [36]

$$(k_{\mathrm{eq}})_j = -\mathrm{i}\sum_{l=1}^{N} C_{jl}P_{lj} \ (P_{lj} = \mathrm{e}^{\mathrm{i}}(l-j)kh). \tag{3.5}$$

In the present paper, the boundary treatment is an optimization process for resolution under the constraints of stability. The stability of the boundary schemes is our main concern, based on which high resolution is also pursued.

First take the 4P3Om1 scheme as the interior scheme for example. Note that the 4P3Om1 scheme may be applied from $j = 2$ to $j = N - 2$. Therefore, it needs boundary schemes only at $j = 1$, $N - 1$ and N in the conventional way. Here we do not match the boundary schemes with the interior schemes by the conventional method because it can not ensure the stability of near-boundary schemes (see Ref. [36]).

The method described below is not hard to handle, and, to our best knowledge, it is brand new.

The following steps detail the procedure for constructing boundary schemes:

(1) For the 1st point (the boundary point), the following scheme is recommended:

$$u'_1 = (-3u_1 + 4u_2 - u_3)/2h. \tag{3.6}$$

(2) For the 2nd point, we suggest an assistant scheme. The assistant scheme is not the one truly used on the 2nd point. However, it has a valuable function. It can be used to produce stable schemes for other points near the boundary. The assistant scheme, shown below (3.7), is an $a - b -$ family of schemes whose accuracy is at least third-order:

$$u_2' = (c_{2,1}u_1 + c_{2,2}u_2 + c_{2,3}u_3 + c_{2,4}u_4 + c_{2,5}u_5 + c_{2,6}u_6)/h, \tag{3.7}$$

where

$$\begin{aligned} c_{2,1} &= 4b + a - 1/3, \\ c_{2,2} &= -15b - 4a - 1/2, \\ c_{2,3} &= 20b + 6a + 1, \\ c_{2,4} &= -10b - 4a - 1/6, \\ c_{2,5} &= a, \\ c_{2,6} &= b. \end{aligned}$$

However, we should note that this assistant scheme is essentially unstable. After all the schemes become stable with the help of the assistant scheme, the assistant scheme will be replaced with another scheme for the sake of the stability of the 2nd point. We recommend the following explicit second-order central difference scheme (3.8) to replace the assistant scheme (3.7),

$$u_2' = (-u_1 + u_3)/2h. \tag{3.8}$$

(3) For the 3rd point near the boundary, the scheme is produced by the combination of the assistant scheme and the interior scheme. For the current case, the interior scheme is 4P3Om1, which has the following form on the 3rd point:

$$u_3' = \left(\frac{1}{h}\sum_{n=-1}^{2} a_{0,n}u_{3+n} - a_{1,-1}u_2'\right)/a_{1,0}. \tag{3.9}$$

Substituting Eq. (3.7) into Eq. (3.9) yields the scheme on the 3rd point with a and b as free parameters. Working on the obtained scheme under the procedure listed in Section 2.1 we can get the scheme with the optimal resolution under the constraints of stability. In this optimization we set $top = 1.0$. The resulting optimal values of a and b are 0.2316635846960722E−08 and −0.8639865391536755E−01. Thus, the scheme for the 3rd point is obtained, which is

$$\begin{aligned} u_3' = {} & 0.3149166539411899\text{E}{+}00u_1 - 0.1552924451942358\text{E}{+}01u_2 \\ & + 0.1229197935024197\text{E}{+}01u_3 - 0.1921363283034527\text{E}{-}01u_4 \\ & - 0.1205200134841980\text{E}{-}01u_5 + 0.4007549715573577\text{E}{-}01u_6. \end{aligned} \tag{3.10}$$

These two values of a and b work well for the 3rd point. However, it does not necessarily mean that this combination of a and b is a good choice for the point $j = 4$ and other successive points. Schemes on near-boundary points are prone to instability, so we should work on them point by point until the property of the scheme on some point approaches that of the interior scheme. In short, the process of constructing the boundary schemes is essentially a continuous transition from the assistant scheme to the interior scheme, so all the boundary schemes are their intermediate versions.

(4) For the 4th point near the boundary, the scheme is developed in a similar manner. On this point, the interior scheme has the following form:

$$u_4' = \left(\frac{1}{h}\sum_{n=-1}^{2} a_{0,n}u_{4+n} - a_{1,-1}u_3'\right) \Big/ a_{1,0}. \tag{3.11}$$

Substituting Eq. (3.7) into Eq. (3.9), and then substituting the obtained (3.9) directly into Eq. (3.11), the scheme on the 4th point is obtained. Free parameters a and b are also included. Optimizing them under the constraints of stability yields $a = 0.8650992966101587\text{E}{-}02$ and $b = 0.3460392329851057\text{E}{-}01$. So we get

$$\begin{aligned} u_4' = {} & -0.4007550301083819\text{E}{-}01u_1 + 0.3223617559816121\text{E}{+}00u_2 \\ & - 0.1222025327151400\text{E}{+}01u_3 + 0.6326604756729091\text{E}{+}00u_4 \\ & + 0.3116855212361244\text{E}{+}00u_5 - 0.4606922728407310\text{E}{-}02u_6. \end{aligned} \tag{3.12}$$

(5) Following the same procedure, we get $a = 0.4522250370424067\text{E}-02$ and $b = 0.2110056888528983\text{E}-01$ for the 5th point and $a = 0.4775523008358158\text{E}+00$ and $b = -0.9528171799374116\text{E}-01$ for point $j = 6$. Using the optimized parameters, we get the following schemes for the 5th and 6th points, respectively.

$$\begin{aligned} u'_5 = {} & 0.2439117258895970\text{E}-01u_1 - 0.1713875409769093\text{E}+00u_2 \\ & + 0.5962531044108447\text{E}+00u_3 - 0.1492293792986813\text{E}+01u_4 \\ & + 0.7473705734300687\text{E}+00u_5 + 0.3077184838077115\text{E}+00u_6 \\ & - 0.1205200027386216\text{E}-01u_7. \end{aligned} \tag{3.13}$$

$$\begin{aligned} u'_6 = {} & -0.1096648176992323\text{E}-01u_1 + 0.7272086997699330\text{E}-01u_2 \\ & - 0.2529357474000156\text{E}+00u_3 + 0.6584785916213984\text{E}+00u_4 \\ & - 0.1508480763411324\text{E}+01u_5 + 0.7434112820192262\text{E}+00u_6 \\ & + 0.3098242492375073\text{E}+00u_7 - 0.1205200027386216\text{E}-01u_8. \end{aligned} \tag{3.14}$$

In the same way, all the schemes on the successive points can be considered as "boundary schemes" and can be optimized for good resolution. However, farther away from the boundary, the influence of the boundary diminishes quickly. On points $7 \leqslant j \leqslant N-2$ there is no need to change these two free parameters because of the good resolution characteristics of these points when the combination of a and b for point $j = 6$ is used. For conciseness, the optimal values of the free parameters are also listed in Table 2.

(6) For points $j = N-1$ and N, we recommend the following scheme expressions:

$$u'_{N-1} = (2u_N + 3u_{N-1} - 6u_{N-2} + u_{N-3})/6h, \tag{3.15a}$$

$$u'_N = (3u_N - 4u_{N-1} + u_{N-2})/2h. \tag{3.15b}$$

So far, all the boundary schemes have been produced. Near the left boundary, there are six boundary schemes, which are (3.6), (3.8), (3.10), (3.12), (3.13) and (3.14). They are used for the points $j = 1, 2, 3, 4, 5$ and 6, respectively. Near the right boundary, only two points need boundary schemes. They are $j = N-1$ and N. Schemes (3.15a) and (3.15b) are used for them.

There is nothing new in the process of calculating the first derivatives, just going through the point $j = 1$ to the point $j = N$. Emphasis is placed on the point $j = 2$ where the scheme used is (3.8), not the assistant scheme (3.7).

For different nodes the real and imaginary parts of $k_{\text{eq}}h$ are obtained from Eq. (3.5) and plotted as a function of kh in Figs. 5 and 6, respectively. Here a value of N is chosen sufficiently large so that the results presented for $k_{\text{eq}}h$ do not depend upon this choice. We use 30 points, with the 1st and the 30th point as boundary points. Since the first derivative in the interior scheme is upwind biased, the best resolution property, namely the resolution closest to the property of the interior scheme, occurs on the 28th point. Fig. 5 shows that the spectral resolution becomes more accurate on the spectral plane as j increases except for the right two boundary points. It is noteworthy that the resolution has been very close to that of the point $j = 28$ when j equals 6. From Fig. 6 we can see that the scheme is stable on every point as expected.

If the 3P3Om2 scheme is taken as the interior scheme, the method for boundary closures is essentially not changed except that not merely the first but also the second derivative of the point $j = 2$ is offered in the assistant scheme. We propose the following assistant expression for the second derivative:

$$u''_2 = (s_{2,1}u_1 + s_{2,2}u_2 + s_{2,3}u_3 + s_{2,4}u_4 + s_{2,5}u_5 + s_{2,6}u_6 + s_{2,7}u_7)/h^2, \tag{3.16}$$

Table 2
Optimized parameters for boundary closures for the 4P3Om1 scheme

	top	*a*	*b*
$j = 3$	1.0	0.2316635846960722E−08	−0.8639865391536755E−01
$j = 4$	1.0	0.8650992966101587E−02	0.3460392329851057E−01
$j = 5$	0.8	0.4522250370424067E−02	0.2110056888528983E−01
$j = 6$	1.5	0.4775523008358158E+00	−0.9528171799374116E−01

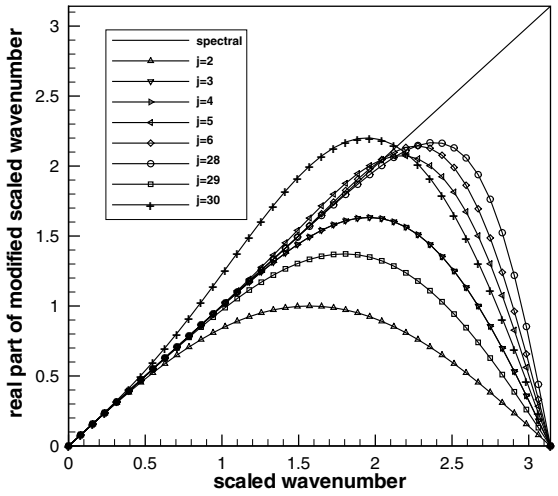

Fig. 5. Real part of $k_{eq}h$ for the first derivative for points $j = 2, 3, 4, 5, 6, 16, 29$ and 30 for the 4P3Om1 scheme.

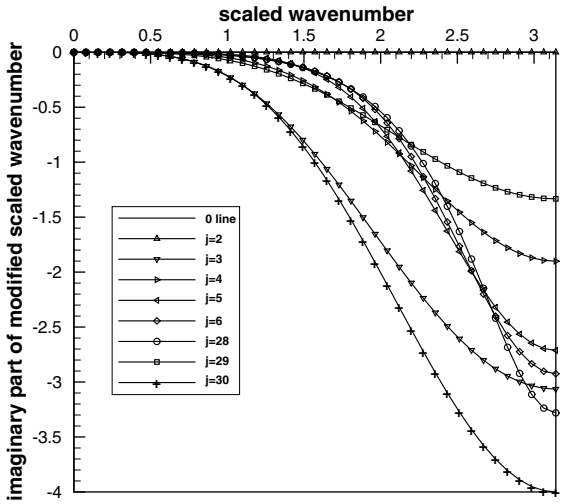

Fig. 6. Imaginary part of $k_{eq}h$ for the first derivative for points $j = 2, 3, 4, 5, 6, 16, 29$ and 30 for the 4P3Om1 scheme.

where

$$s_{2,1} = -g - 5q + 11/12,$$
$$s_{2,2} = 5g + 24q - 5/3,$$
$$s_{2,3} = -10g - 45q + 1/2,$$
$$s_{2,4} = 10g + 40q + 1/3,$$
$$s_{2,5} = -5g - 15q - 1/12,$$
$$s_{2,6} = g,$$
$$s_{2,7} = q.$$

Following the same procedures listed above, we can get schemes with good resolution satisfying the constraints of stability on the near-boundary points. The optimization results of free parameters are listed in Table 3. Boundary schemes (3.6) and (3.15b) are used on the left and right boundary points. For the 2nd point we also recommend the explicit second-order central difference Scheme (3.8).

Table 3
Optimized parameters for boundary closures for the 3P3Om2 scheme

	top	*a*	*b*	*g*	*q*
$j=3$	1.0	-0.1490028782144423E−05	−0.2161896888074244E+00	0.1222489959707739E−01	−0.4171400590339880E+00
$j=4$	1.0	0.9168425800492562E−02	0.3667370129576726E−01	0.2663926459408015E−03	0.1598356508751940E−02
$j=5$	1.2	0.5462352011564656E+00	−0.1045420416167275E+00	0.1187901591785011E+00	0.4980439891685980E+00
$j=6$	1.5	0.5128715797018083E+01	−0.9974972133950721E+00	0.9542820125620346E+00	−0.5203265448047872E+01
$j=7$	1.5	0.1876948339134585E+01	−0.3608498048611949E+00	0.3770446571440025E+00	−0.1356626188389042E+01

If the 7P7Om2 scheme is used on the interior points, the method for boundary closures is essentially the same as that for the 3P3Om2 scheme. (Details can be found in Appendix B.)

Due to the constraints of stability on every point, the schemes proposed in this paper are third-order accurate globally (second-order at boundaries) on a uniform grid when the boundary conditions are non-periodic. However, through optimization, the proposed schemes are designed to possess enhanced spectral resolution. The property of good spectral resolution of a scheme is quite important in fields such as aeroacoustics and turbulence simulations. From Fig. 5, we can learn that the resolution of the near-boundary points is worse than that of the interior points. So it is suggested that the mesh should be slightly clustered near the boundary on the physical plane to pursue global high spectral accuracy.

Because there is no anti-diffusion on any point, FS-stability is stricter than time stability. Also, considering that, multiplying the obtained derivatives by metric coefficients does not change the stability property of any point, we can conclude that the schemes proposed above are FS-stable and are therefore also asymptotically stable on a stretched grid with arbitrary strength. However, the schemes that only possess time stability may become time unstable when the grid is stretched, so FS-stable schemes have a substantial advantage over other schemes in regard to such problems that involve complex geometries on the physical plane, where clustered meshes are often adopted.

3.2. Numerical verification

In this section, we use numerical solutions of the advection equation to identify the boundary closures that yield stable solutions over long time periods.

Consider the one-dimensional advection equation, $u_t + u_x = 0$, with initial conditions $u_0(x) = \sin(\pi x)$, defined on $[-1, 1]$ with boundary conditions $u(-1, t) = \sin(\pi(-1 - t))$. Note that the exact solution to the above equation is given by $u_{\text{exact}}(x, t) = \sin(\pi(x - t))$.

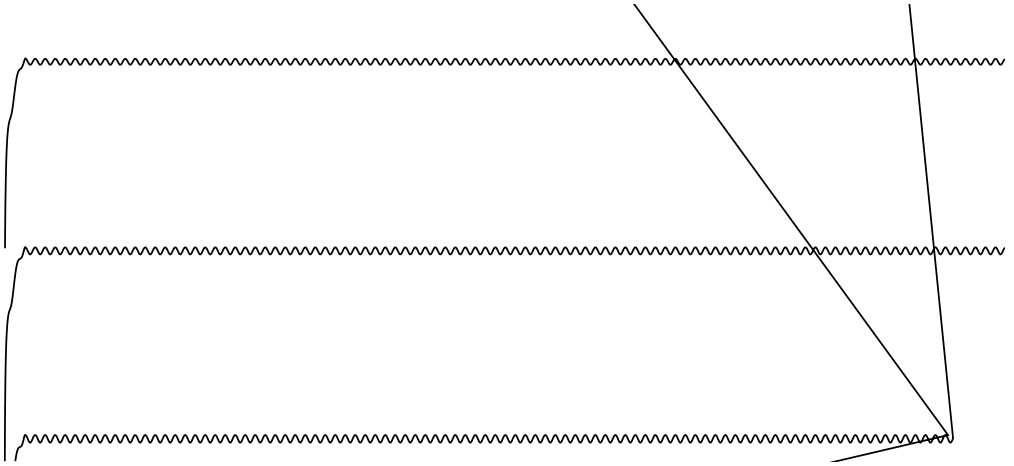

The time integration is performed by means of a three-stage, TVD Runge–Kutta scheme [54], which is also adopted in all other numerical tests in the present paper. A uniform mesh with three different resolutions is used for spatial discretization. Setting the CFL number to 0.1, we integrate the solution to $t = 100$. Note that the solution travels one wavelength in two time units. The L_2 error, $\sqrt{1/N\sum_{j=1}^{N}(u_j - u_{\text{exact}})^2}$, is then examined for boundedness. Fig. 7 illustrates the stability of the proposed schemes. It can be seen that the combinations of the boundary and interior schemes are asymptotically stable. After a simple approximate estimate, it is also clear that the formal accuracy of these schemes is third-order, one order higher than the scheme presented by Sengupta et al. [52], who, to our best knowledge, were the first to consider FS-stability in Ref. [36].

4. Hybridization for shock-capturing

4.1. Hybridization strategy

Compact schemes are very accurate in smooth regions with spectral-like resolution, but they have been found to cause non-physical oscillations when they are applied directly to flows with discontinuities. The non-physical oscillations (Gibbs' phenomena) do not decline in magnitude when the grid is refined. Several approaches have been proposed to overcome this difficulty. For a detail review the reader is referred to [39]. Pirozzoli [45] has derived a hybrid compact-WENO scheme in which a conservative compact scheme is developed to be coupled with the WENO scheme. The hybrid compact-WENO scheme generally outperforms Adams and Shariff's [40] compact-ENO scheme in the sense that the WENO scheme yields higher accuracy than the ENO scheme at almost the same price. Ren et al. [39] considered the hybrid scheme as the weighted average of two sub-schemes: the conservative compact scheme proposed by Pirozzoli [45] and the WENO scheme. The weight function is designed to be continuous so that the abrupt transition from one sub-scheme to another is avoided. Also, it is pertinent to mention that a switching function [46], named the Jameson–Schmidt–Turkel switch (JST switch) after the inventors' names by later investigators, has earlier been proposed for a scalar dissipation model. The JST switch can be interpreted as a limiter. It activates the dissipation term (usually the second-difference term) at not only discontinuities but also extrema in the smooth region, which is too dissipative for high-resolution calculations. A novel switch based on second derivatives was introduced by Sengupta et al. [50]. The method was very simple and was proven to be effective for diagnosing the discontinuity of the Burgers equation. However, the threshold value must be selected cautiously, because the threshold depends on the problem being solved. For example, a threshold value of 50 (recommended by the author) may be suitable for the 1-D sine wave, $\sin(x)$. But when it is used to simulate another smooth wave, $\sin(20x)$, which inherently has larger second derivatives, many points will be misdiagnosed as discontinuities. It also should be noted that this problem can not be fixed by refining the mesh. Additionally, second derivatives as well as first derivatives oscillate from extreme positive values to extreme negative values near discontinuities. Between the negative and positive extrema there exist second derivatives with relatively small amplitudes. So, when a discontinuity comes up, the recommended upwind schemes might not be patched in a continuous manner, but a staggered manner. The ruleless abrupt change of schemes may result in unknown source terms with an unknown nature in the difference equation.

The drawback of the smoothness indicator in Ref. [39] is that it may mistake some points in smooth waves for discontinuity points, especially in high-wavenumber waves. This issue is addressed in detail in the following description of the hybridization process. In order to counter this deficiency, we identify the discontinuity in two steps, where the details in the first step are almost the same as those in Ref. [39]. In the second step, a new discontinuity indicator is adopted to pick out these points, which are taken as discontinuity in the preceding step. The adoption of the second step only incurs a little computational cost; however, it can significantly enhance the resolution of the solution.

In the present paper, the compact scheme can be expressed in the following form (h is set to 1 for simplicity in the computation domain):

$$AU_{j-1} + BU_j = D_j, \tag{4.1}$$

where

$$U_j = \begin{bmatrix} u'_j \\ u''_j \end{bmatrix}, \quad D_j = \begin{bmatrix} \sum_{n=-k_1}^{k_2} a_{0,n} u_{j+n} \\ \sum_{n=-k_1}^{k_2} \bar{a}_{0,n} u_{j+n} \end{bmatrix}, \quad A = \begin{bmatrix} a_{1,-1} & a_{2,-1} \\ \bar{a}_{1,-1} & \bar{a}_{2,-1} \end{bmatrix}, \quad B = \begin{bmatrix} a_{1,0} & a_{2,0} \\ \bar{a}_{1,0} & \bar{a}_{2,0} \end{bmatrix}. \tag{4.2}$$

Also the WENO scheme can be expressed in this form:

$$B' U_j = D'_j, \tag{4.3}$$

where

$$U_j = \begin{bmatrix} u'_j \\ u''_j \end{bmatrix}, \quad D'_j = \begin{bmatrix} \hat{f}^{\mathrm{WENO}}_{j+1/2} - \hat{f}^{\mathrm{WENO}}_{j-1/2} \\ f^{(2)}_j \end{bmatrix}, \quad B' = \begin{bmatrix} 1 & 0 \\ 0 & 1 \end{bmatrix}. \tag{4.4}$$

The $\hat{f}^{\mathrm{WENO}}_{j+1/2}$ in expression (4.4) denotes the flux function of the WENO scheme, while $f^{(2)}_j$ denotes the explicit central difference scheme for the second derivative on the jth node. For the 3P3Om2 and 4P3Om1 schemes, the WENO-3 scheme (third-order accurate at discontinuities and fifth-order accurate in the smooth region) [42] is chosen for hybridization, while for 7P7Om2, the MPWENO-5 scheme (fifth-order accurate at discontinuities and ninth-order accurate in the smooth region) [41] is employed. As regards $f^{(2)}_j$, the fourth-order and sixth-order explicit central schemes are adopted for 3P3Om2 and 7P7Om2, respectively.

Multiplying Eq. (4.1) by σ_j and Eq. (4.3) by $1 - \sigma_j$, and adding the results together, we have

$$\sigma_j A U_{j-1} + (\sigma_j B + (1 - \sigma_j) B') U_j = \sigma_j D_j + (1 - \sigma_j) D'_j. \tag{4.5}$$

Eq. (4.5) is reduced to a compact scheme if $\sigma_j = 1$ and to the WENO scheme if $\sigma_j = 0$. According to the spirit of the hybrid scheme, it is necessary that the weight be directly related to the smoothness of the numerical solution. The process of defining the weight function σ is as follows:

(1) The smoothness indicator is designed to be [39]

$$r_j = \frac{|2\Delta f_{j+1} \Delta f_j| + \varepsilon}{(\Delta f_{j+1})^2 + (\Delta f_j)^2 + \varepsilon}, \tag{4.6}$$

where $\Delta f_j = f_j - f_{j-1}$. The ε is a positive real number to avoid possible division by zero. Following Ren et al.'s [39] method, we choose ε in the formula

$$\varepsilon = \frac{0.9 r_c}{1 - 0.9 r_c} \xi^2. \tag{4.7}$$

In Eq. (4.7), ξ acts as a threshold value. All fluctuations smaller than this value will be considered as turbulent fluctuations and will not be damped by using the WENO scheme. For a detailed description of Eq. (4.7), the reader is referred to [39]. It is apparent that $r_j \in [0, 1]$ and this will facilitate the choice of the threshold value r_c (see Eq. (4.8)). In this step the weight takes the following form [39]:

$$\sigma_j = \min\left(1, \frac{r_j}{r_c}\right). \tag{4.8}$$

In our tests, ξ and r_c are set to be 1×10^{-4} and 0.6, respectively.

(2) We propose the following criterion to filter out these points around which smooth waves exist. The criterion is applied only on points where σ_j is less than 1.

If both

$$\alpha_1(|\Delta f_j| + \beta_1 |\Delta f_{j-1}| + \beta_1 |\Delta f_{j-2}|) > |\Delta f_{j+1}| \tag{4.9}$$

and

$$\alpha_2(|\Delta f_{j+1}| + \beta_2 |\Delta f_{j+2}| + \beta_2 |\Delta f_{j+3}|) > |\Delta f_j| \tag{4.10}$$

hold true, σ_j is modified to 1; otherwise σ_j is set to 0. Note that $\beta_1 > 1, \beta_2 > 1, \alpha_1(1 + 2\beta_1) > 1$, $\alpha_2(1 + 2\beta_2) > 1$, in inequalities (4.9) and (4.10).

In step 1, we have learned that the ratio of $|\Delta f_{j+1}|$ to $|\Delta f_j|$ is much greater or less than one if $\sigma_j < 1$. However, this does not necessarily mean that a discontinuity exists around point j. In Fig. 8, sine waves with wavenumbers $kh = \frac{3\pi}{5}$ and $kh = \frac{\pi}{5}$ are shown respectively. After step 1, we get $\sigma_j < 1$ on points $j = 3, 4, 8, 9, 13, 14, 18, 19, 23$ and 24, where the function u is still smooth. If WENO schemes are applied on these points, it will produce noticeable dispersion and dissipation errors and the solution may be contaminated, so more information should be introduced from points in the neighborhood for the discontinuity diagnosis. This is why $|\Delta f_{j-1}|, |\Delta f_{j-2}|, |\Delta f_{j+2}|$ and $|\Delta f_{j+3}|$ show up and have larger weights ($\beta_i > 1,\ i = 1, 2$) than $|\Delta f_j|$ and $|\Delta f_{j+1}|$ in this criterion. The weight sums of the LHS of inequalities (4.9) and (4.10), which are controlled by the value of parameters α_i and β_i ($i = 1, 2$), should both be greater than 1, or we can not ensure that discontinuity exists when any one of the inequalities fails. So $\alpha_i(1 + 2\beta_i) > 1$ ($i = 1, 2$) should be satisfied. For simplicity and no loss of generality, we only discuss on the case of $|\Delta f_j| > |\Delta f_{j+1}|$. Under this condition, if inequality (4.9) does not hold true, it implies that the average of $|\Delta f_{j-1}|$ and $|\Delta f_{j-2}|$ is smaller than $|\Delta f_{j+1}|$, so $|\Delta f_j|$ is the greatest one. We can conclude that probably a discontinuity exists near the point j. If expression (4.9) is satisfied, then we go on to check the inequality (4.10). If inequality (4.10) also holds true, which means that $|\Delta f_j|$ is not much greater than $|\Delta f_{j+2}|$ or $|\Delta f_{j+3}|$, we can arrive at the conclusion that there exists a smooth wave around this point; otherwise the information that $|\Delta f_j|$ is much greater than $|\Delta f_{j+2}|$ and $|\Delta f_{j+3}|$ can be

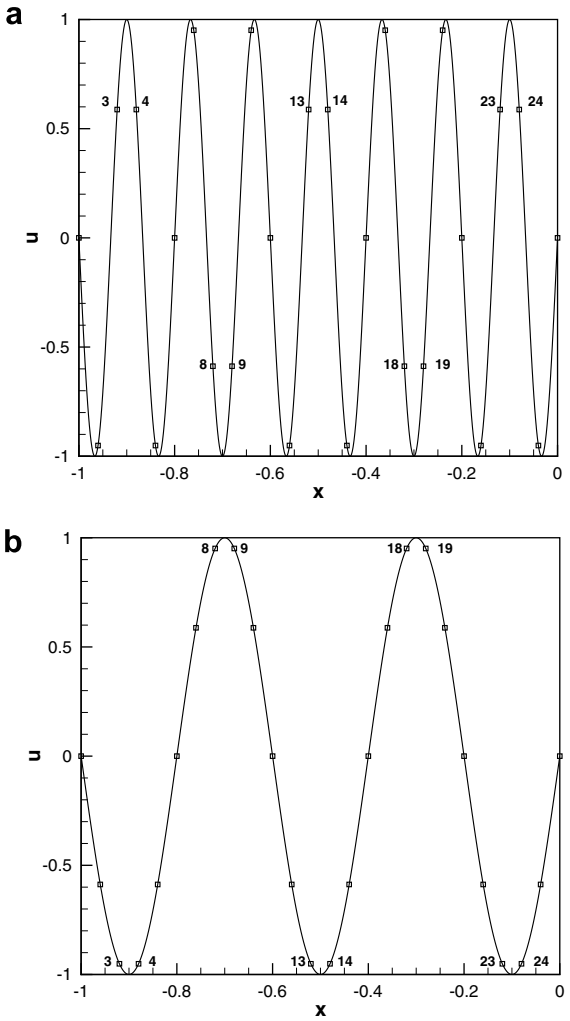

Fig. 8. Illustration for points that can be taken as discontinuities following the method in Ref. [39]: (a) $kh = \frac{3\pi}{5}$; (b) $kh = \frac{\pi}{5}$.

obtained, which means that there is a discontinuity near the point j. The α_i and β_i $(i = 1, 2)$ in the criterion are parameters that can be adjusted for different strengths of discontinuity. Generally speaking, the discontinuity we capture becomes stronger with the increase of α_i and β_i $(i = 1, 2)$. Numerical tests show that the combination of $\alpha_1 = 0.15, \alpha_2 = 0.3$ and $\beta_1 = \beta_2 = 5$ works well.

After these two steps are executed, the weight function σ_j is set to 0 only when the real discontinuity shows up with the strength of some level measured by $\alpha_i(1 + 2\beta_i) > 1$ $(i = 1, 2)$ or even stronger; otherwise it is changed to 1. The reason for these actions is that we expect the compact sub-scheme that has the property of good dispersion relation preservation to dominate the hybrid scheme. In order to avoid the non-smooth transition between the sub-schemes, the weight can be smoothed in the following simple way.

The weights near the point where $\sigma_j = 0$ are modified using the expression

$$\sigma_{j+i} = \max(0, \sigma_{j+i} - (1 - \sigma_j)\exp(-\gamma|i|)), \tag{4.11}$$

where

$$(i = -m_1 \cdots m_2, i \neq 0). \tag{4.12}$$

Indices m_1 and m_2 are used to confine the domain affected by the discontinuity, and the parameter γ is used to adjust the influence on the neighbor weights when discontinuity occurs. Numerical tests show that $m_1 = 3$ and $m_2 = 1$ work well for the 4P3Om1 and 3P3Om2 schemes, and that $m_1 = 4$ and $m_2 = 3$ work well for the 7P7Om2 scheme. Numerical tests also show that $\gamma = 1$ is an appropriate choice for all these schemes.

4.2. Numerical tests for proposed hybridization strategy

In the following, two numerical tests are executed to confirm the high level of fidelity of the present hybridization method. For convenience, we label the hybrid schemes only using the names of the corresponding compact schemes.

(1) We consider the scalar model problem with periodic boundaries:

$$\begin{aligned} &u_t + u_x = 0, \quad -1 \leqslant x \leqslant 1, \ \ t > 0, \\ &u(x, 0) = \sin(30\pi x), \quad -1 \leqslant x \leqslant 1. \end{aligned} \tag{4.13}$$

Two tests are executed in this case, where the 7P7Om2 scheme hybridized with the MPWENO-5 scheme is employed. In the first test, the proposed hybridization method is adopted, which concludes step 1 and 2. In the second test, only step 1 is executed for calculating the weights. Using a uniform mesh with 101 points, we advance the time to $t = 0.5$. The results are shown in Figs. 9(a) and (b), and the results from the MPWENO-5 scheme are also provided for comparison. Due to the built-in dissipation, the waves are all attenuated in amplitude. From Fig. 9(a) we can see that, in the step 1 case, both the dispersion error and the dissipation error are larger than those of the step 1_2 case. Obviously, the unwanted enlarged errors come from the combined MPWENO-5 schemes. Fig. 10 plots the distribution of the weight σ in both the first and last time step. We can see that the weights equal one on all points in the step 1_2 case, while the weights on about 40% of the points are less than one in the step 1 case; namely, some points in smooth waves are recognized as points of discontinuity. And what's more, the computation becomes more time-consuming.

(2) Our next test problem consists of testing the behavior of the scheme on a rather stringent scalar advection test problem. This is the same test problem that was catalogued in Jiang and Shu [53]. Thus we solve the problem

$$\begin{aligned} &\frac{\partial u}{\partial t} + \frac{\partial u}{\partial x} = 0, \\ &u(x, 0) = u_0(x), \quad \text{periodic} \end{aligned} \tag{4.14}$$

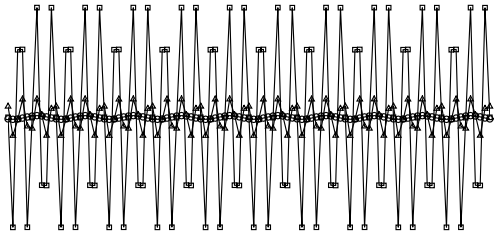

with

$$
\begin{aligned}
u_0(x) &= \frac{1}{6}[G(x,\beta,z-\delta) + G(x,\beta,z+\delta) + 4G(x,\beta,z)], \quad -0.8 \leqslant x \leqslant -0.6;\\
&= 1, \quad -0.4 \leqslant x \leqslant -0.2;\\
&= 1 - |10(x-0.1)|, \quad 0 \leqslant x \leqslant 0.2;\\
&= \frac{1}{6}[F(x,\alpha,a-\alpha) + F(x,\alpha,a+\alpha) + 4F(x,\alpha,a)], \quad 0.4 \leqslant x \leqslant 0.6;\\
G(x,\beta,z) &= \mathrm{e}^{-\beta(x-z)^2};\\
F(x,\alpha,a) &= \sqrt{\max(1-\alpha^2(x-a)^2, 0)}.
\end{aligned}
\tag{4.15}
$$

The constants in Eqs. (4.15) are given by

$$
a = 0.5; \quad z = -0.7; \quad \delta = 0.005; \quad \alpha = 10; \quad \beta = \frac{\log 2}{36\delta^2}.
$$

This is a stringent test problem because it has a combination of functions that are not smooth and functions that are smooth but sharply peaked. The problem is initialized on a mesh of 400 zones. It is run for a

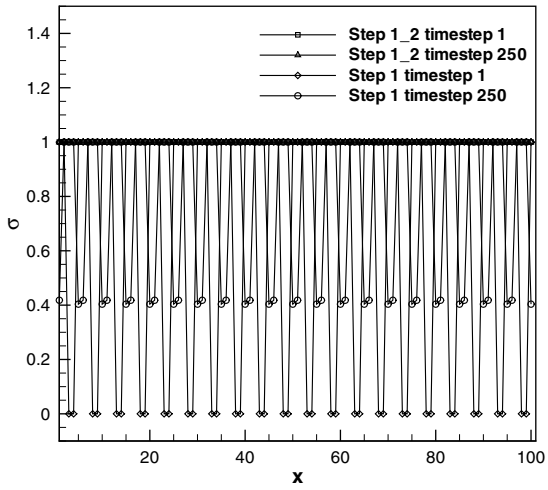

Fig. 10. Illustration of σ distributions at both the first and last time step for step 1 and step 1_2 cases.

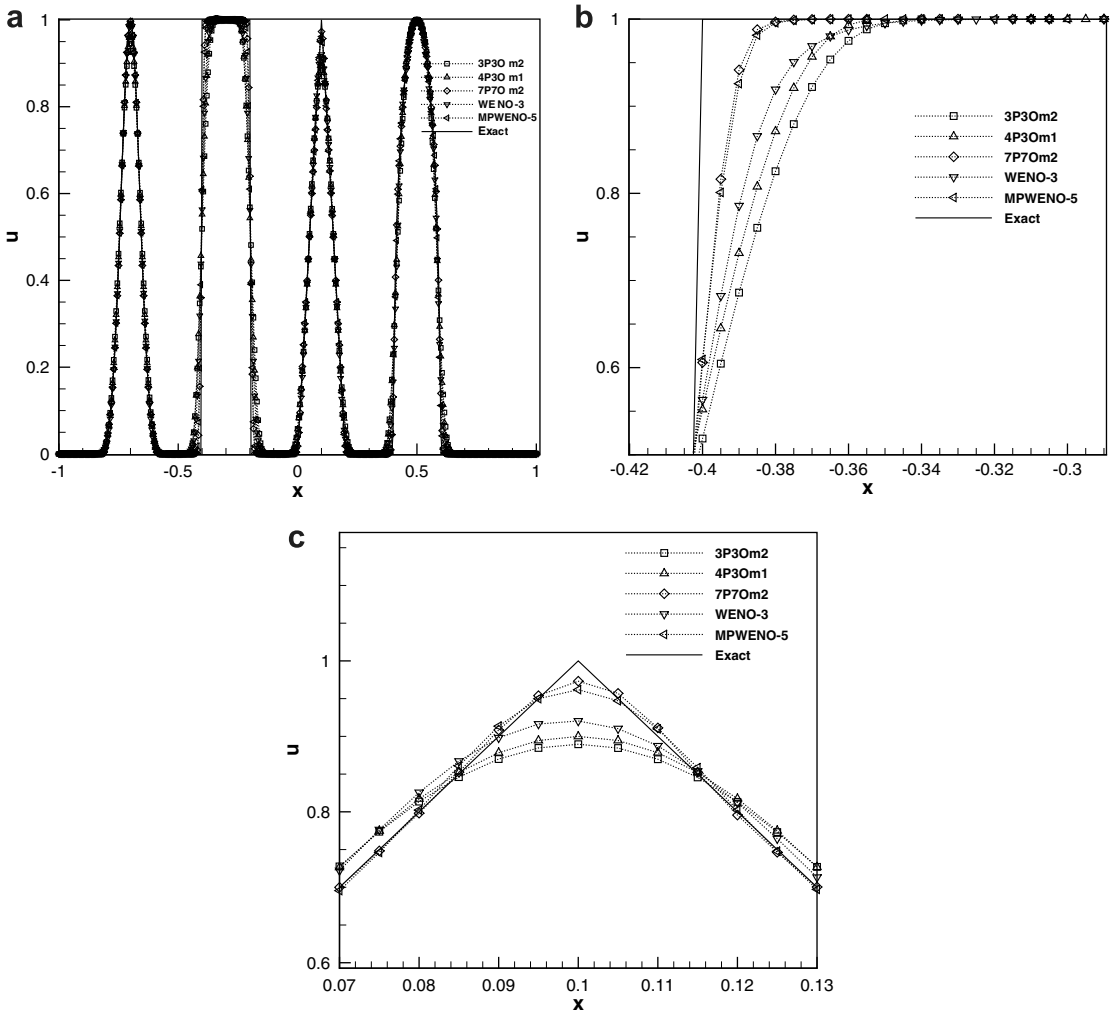

Fig. 11. (a) Computation results of linear wave equation; third-order Runge–Kutta in time; 400 points, CFL = 0.1; (b) magnification of part of (a); (c) magnification of part of (a).

simulation time of 10, which corresponds to five traversals around the mesh. In doing so, the features catalogued in Eqs. (4.15) are advected over 2000 mesh points. The problem is run with a CFL number of 0.1.

In Fig. 11(a) we show the results from the proposed hybrid schemes. The results from WENO-3 and MPWENO-5 and the exact solution are also shown in the figure for comparison. It can be seen that the different shapes have been accurately advected. Notice, too, that the profiles of all the pulses are almost symmetrical about their peaks, which is a very desirable feature in a numerical algorithm. Figs. 11(b) and (c) show the magnifications of the numerical solution. We can see that the square wave profile has become sharper than the MPWENO-5 scheme when the primary scheme is 7P7Om2 in the hybrid scheme. Also the triangular pulse is the most acute when 7P7Om2 is adopted. The 3P3Om2 and 4P3Om1 schemes also perform very well in this rather stringent test. It can be seen that both of them are a little more dissipative than the WENO-3 scheme, which is due to their third-order accuracy.

In Fig. 12, the distributions of the weight σ at the last time step with respect to the mesh points from 1 to 400 are shown. It is clear that the proposed compact schemes overwhelmingly dominate the computation even in this rather stringent test. The percentages of the zero weight for the 7P7Om2, 3P3O2 and 4P3Om1 cases are about 8%, 3% and 2%, respectively.

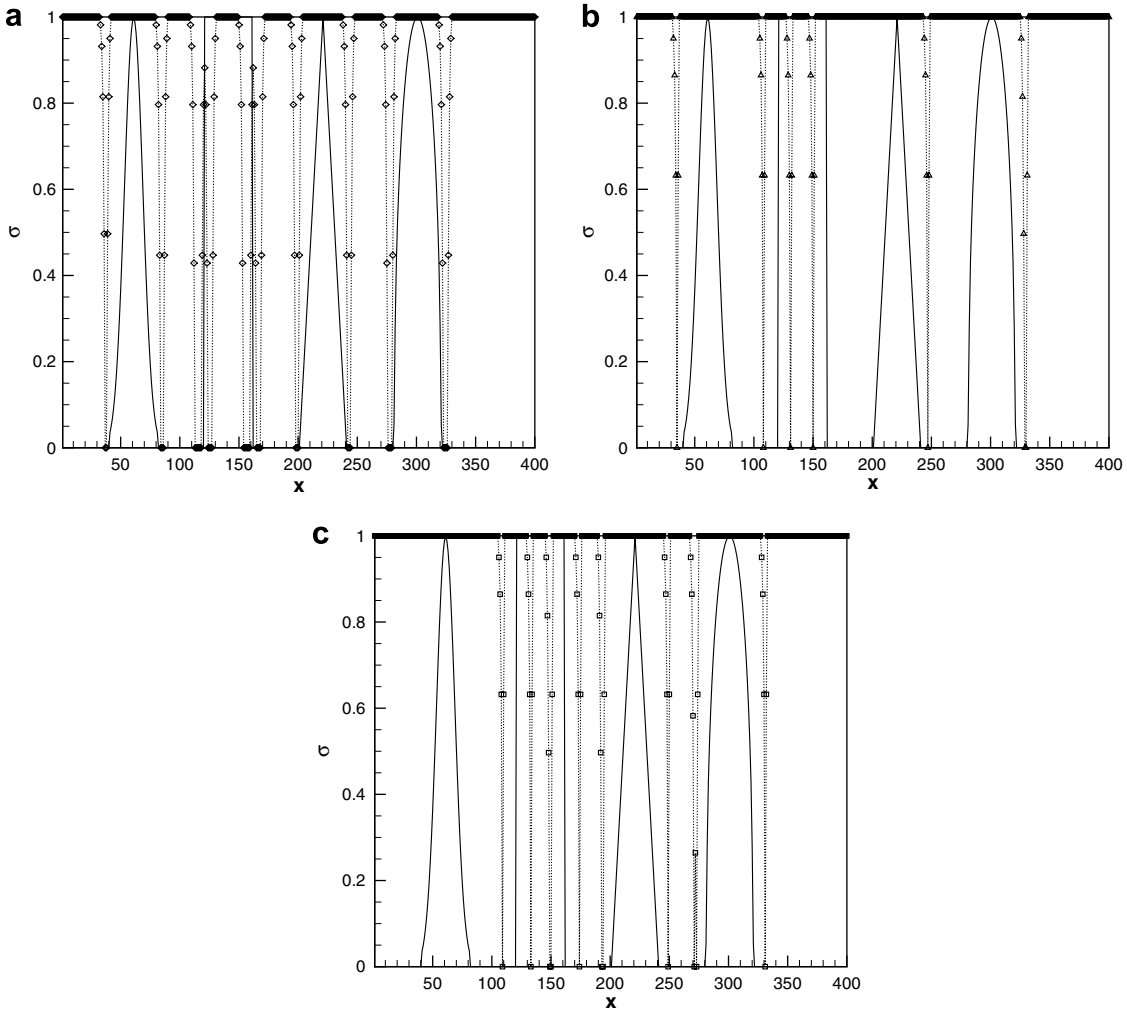

Fig. 12. Distributions of σ at the last time step of the time $t = 10$. The compact schemes in the hybrid scheme are (a) 7P7Om2, (b) 4P3Om1, (c) 3P3Om2, respectively.

5. Cost comparison

Often compact schemes are used in the simulation of complex flows with shock waves. Therefore, in this section, the computational cost of the hybrid schemes proposed is assessed and compared to that of the standard Pade schemes. Assuming that the solution is smooth in most of the field, we execute the comparison as follows.

All the schemes concerned here are hybridized with WENO schemes for shock-capturing by the means listed in Section 4.1. For convenience, we distinguish the hybrid schemes using the names of the corresponding compact schemes. We do not consider the operations for calculating fluxes using WENO schemes because they are almost the same when the same criterion is used for identifying discontinuity. We do not count the operations for boundary treatment either, because these operations can be omitted when the number of points used in the domain of computation is large.

The standard Pade schemes are of the form

$$Au' = Bu, \tag{5.1}$$

where $u = [\dots u_{j-1}, u_j, u_{j+1}, \dots]^{\mathrm{T}}$ and $u' = [\dots u'_{j-1}, u'_j, u'_{j+1}, \dots]^{\mathrm{T}}$. A is a tri-diagonal matrix when the boundary condition is non-periodic. Note that A and B are not constant matrices here because of hybridization. System (5.1) is solved using the tri-diagonal matrix algorithm (TDMA) [64,65] for high efficiency. For periodic boundary conditions, matrix A is periodic tri-diagonal so the efficient algorithm CTDMA [66] is used.

Using the 4P3Om1 scheme as the interior scheme, for non-periodic boundary conditions we have the following form of equations on every interior node:

$$u'_j = \sum_{n=-1}^{2} a_{0,n} u_{j+n} - a_{1,-1} u'_{j-1}. \tag{5.2}$$

For periodic boundary conditions, system (2.13) is applied.

If the interior scheme is the 3P3Om2 or 7P7Om2 scheme, for non-periodic boundary conditions we have

$$u'_j = \tilde{a}_{1,-1} u'_{j-1} + \tilde{a}_{2,-1} u''_{j-1} + \sum_{n=-1}^{k} \tilde{a}_{0,n} u_{j+n}, \tag{5.3a}$$

$$u''_j = \widetilde{\tilde{a}}_{1,-1} u'_{j-1} + \widetilde{\tilde{a}}_{2,-1} u''_{j-1} + \sum_{n=-1}^{k} \widetilde{\tilde{a}}_{0,n} u_{j+n} \tag{5.3b}$$

on every interior node ($k = 1$ for 3P3Om2 and $k = 5$ for 7P7Om2). For periodic boundary conditions block matrices will be solved. The strategies for these solutions have been illustrated in Section 2.4. The operation count per node with boundary conditions is shown in Table 4. Note Total2 = Total1 + (6 + 3), where (6 + 3) is the number of operations performed when the proposed criterion for discontinuity is executed. Total2 operations are used in real calculations. Obviously, the 4P3Om1 scheme is the fastest one.

The operation count per node with periodic boundary conditions is shown in Table 5. It can be seen that, while 3P3Om2 and 7P7Om2, to some degree, are more time-consuming than other schemes, the 4P3Om1 scheme is still the fastest one. Also, the strategies proposed in Section 2.4 can be implemented in the periodic case when the grid number is adequately large, which will reduce the computational cost by about 40%. The

Table 4
Operation count per node with boundary conditions

	LHS	RHS	Total1	Total2
Pade4	5 + 3[a]	1 + 1	6 + 4	12 + 7
Pade6	5 + 3	2 + 2	7 + 5	13 + 8
4P3Om1	0 + 0	5 + 4	5 + 4	11 + 7
3P3Om2	0 + 0	10 + 8	10 + 8	16 + 11
7P7Om2	0 + 0	18 + 16	18 + 16	24 + 19

[a] The entries are of the form, "number of multiples/divisions + adds/subtracts".

Table 5
Operation count per node with periodic conditions

	LHS	RHS	Total1	Total2
Pade4	10 + 6	1 + 1	11 + 7	17 + 10
Pade6	10 + 6	2 + 2	12 + 8	18 + 11
4P3Om1	5 + 2 (2 + 1)	4 + 3	9 + 5 (6 + 4)[a]	15 + 8 (12 + 7)
3P3Om2	40 + 22 (16 + 9)	5 + 3	45 + 25 (21 + 12)	51 + 28 (27 + 15)
7P7Om2	40 + 22 (16 + 9)	12 + 10	52 + 32 (28 + 19)	58 + 35 (34 + 22)

[a] Datum enclosed in parentheses denote the operation count per node when the number of points in the computational domain is very large.

operation count per node for the proposed schemes with large grid numbers is shown enclosed in parentheses in Table 5.

We suggest the 4P3Om1 scheme for laminar-related problems because of its high efficiency, especially when the flow is smooth, in which case no hybridization is needed and therefore the computational cost is only 1/5 and 1/3 of that of the 7P7Om2 scheme with periodic and non-periodic schemes respectively (see Tables 4 and 5). For turbulence-related problems, the 7P7Om2 scheme is recommended because of its high spectral accuracy. The Pade schemes are not recommended here because they are not as fast as the 4P3Om1 scheme, and they are much less accurate than the 7P7Om2 scheme in the spectral space. Furthermore, Pade schemes require stabilizing filters to suppress poorly resolved waves because of the non-dissipation property, which incurs more computational cost.

6. Numerical tests

A series of numerical tests of scalar problems have been presented in the above paragraphs. The proposed schemes were also tested in some complicated cases, the inviscid Burgers equation, 2-D and 3-D N–S equations respectively. In the following tests, if not noted otherwise, both 4P3Om1 and 3P3Om2 are hybridized with the WENO-3 scheme, while 7P7Om2 is hybridized with the MPWENO-5 scheme. For convenience, we use the names of the compact schemes to denote the corresponding hybrid schemes.

6.1. Inviscid Burgers equation

This equation is used as the first case of a nonlinear equation and can be written as $\frac{\partial u}{\partial t} + u\frac{\partial u}{\partial x} = 0$, subject to the initial condition $u(x,0) = 0.3 + 0.7\sin(\pi(x+1))$ with a periodic boundary condition defined on the domain $-1 \leqslant x \leqslant 1$.

The Lax-Friedrichs splitting method is used, in which $f^{\pm}(u) = (f(u) \pm au)/2$ and $a = \max_u(f'(u))$. Fig. 13 shows the results at $t = 2/\pi$ by using only the proposed compact schemes, not their corresponding hybrid versions. Strong Gibbs' phenomena appear at the discontinuity with all these three schemes. The influences of Gibbs' phenomena are confined in about three points on both sides when the 4P3Om1 and 3P3Om2 schemes are used. But for the 7P7Om2 scheme, which has a wider stencil, the influence spreads away to about ten points on both sides. Fig. 14(a) shows the results at $t = 2/\pi$ with several different schemes. It can be seen that there are essentially no Gibbs' phenomena when WENO-3 and MPWENO-5 schemes are used to solve this problem. Also, strong Gibbs' phenomena disappear when our compact schemes are hybridized. For a clearer picture, see Fig. 14(b), the local enlarged plot of Fig. 14(a), which illustrates the proposed schemes' capability of capturing discontinuities. The curve computed by 4P3Om1 is basically between the curves computed by WENO-3 and MPWENO-5, which is not a bad result for a third-order scheme. However, the curve obtained from 3P3Om2 is almost the flattest one, a bit flatter than that from WENO-3. This may be ascribed to its relatively higher inherent numerical viscosity. The 7P7Om2 scheme attracts more attention because of its excellent performance, which is even better (sharper) than MPWENO-5. Near the discontinuity, MPWENO-5 is brought in by hybridization for good shock-capturing. The numerical dissipation, as a result, is a combination of that of 7P7Om2 and MPWENO-5. Due to 7P7Om2's lower dissipation, it is certain that the result

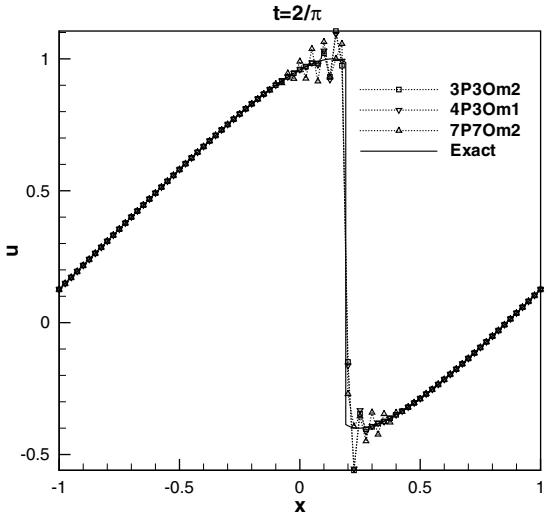

Fig. 13. Gibbs' phenomena when compact schemes 3P3Om2, 4P3Om1 and 7P7Om2 are used to solve the inviscid Burgers equation. $N = 81, t = 2/\pi$.

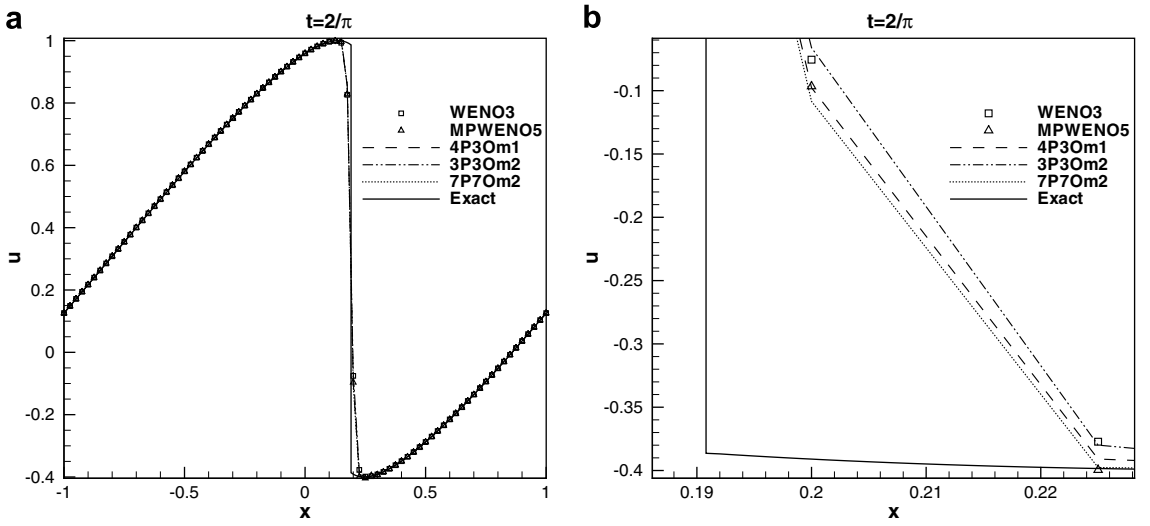

Fig. 14. (a) Numerical results of inviscid Burgers equation, $N = 81, t = 2/\pi$. The compact schemes used here are their hybrid versions. (b) Local enlarged part of (a).

dissipation is lower than that of MPWENO-5. From this test, it can be concluded that the shock-capturing method proposed in this paper performs well for nonlinear problems.

6.2. Shock-wave/boundary-layer interaction

In this test case, an oblique shock wave is made to impinge on a laminar boundary layer that has been developing on a flat plate. The impingement causes the boundary layer to separate at the shock impinging point, which subsequently reattaches, thus creating a separation bubble while maintaining laminar flow conditions throughout. The Mach number upstream of the shock is $M_\infty = 2.0$, and the corresponding shock angle is 32.49°. The Reynolds number, $Re_\infty = 2.96 \times 10^5$, is based on the upstream velocity and the shock impingement distance on the flat plate for an inviscid flow. A schematic diagram of the flow geometry is shown in Ref.

[43] (see Ref. [44] for more details). Computations are carried out on a mesh with (101×55) grid points that are uniform in the stream-wise direction, but clustered in the transverse direction close to the flat plate. Based on the Steger–Warming [55] flux vector splitting, three tests are executed, using 4P3Om1, 3P3Om2 and 7P7Om2 for space discretization of the convective flux, respectively. The diffusive flux terms of the Navier–Stokes equations are discretized by the explicit central fourth-order scheme when 4P3Om1 and 3P3Om2 are adopted, and, for the 7P7Om2 case, the explicit central eighth-order scheme is chosen.

Fig. 15 shows the coefficient of skin-friction C_f in comparison with the experimental data [67]. The filled symbols in Fig. 15, which represent the experimental data of negative values for the C_f in the separated flow region, indicate that their magnitudes have not been measured and have been set to zero for convenience. The numerical results including the separation location and length agree favorably with the experimental data. This good agreement indicates that our hybrid schemes have good shock-capturing properties. It also demonstrates that the boundary closures proposed in virtue of the assistant scheme are successful in practice.

6.3. Shock–vortex interaction

This problem describes the interaction between a stationary shock and a vortex. The computational domain is taken to be $[0,2] \times [0,1]$. A stationary Mach 1.1 shock is positioned at $x = 0.5$ and normal to the x-axis. A small vortex is superposed to the flow left of the shock and centered at $(x_c, y_c) = (0.25, 0.5)$. Referring to Ref. [53], we describe the vortex as a perturbation to the velocity (u, v), temperature $(T = p/\rho)$, and entropy $(S = \ln(p/\rho^\gamma))$ of the mean flow and we denote it by the tilde values:

$$\tilde{u} = \varepsilon\tau e^{\alpha(1-\tau^2)} \sin\theta,$$
$$\tilde{v} = -\varepsilon\tau e^{\alpha(1-\tau^2)} \cos\theta,$$
$$\tilde{T} = -\frac{(\gamma-1)\varepsilon^2 e^{2\alpha(1-\tau^2)}}{4\alpha\gamma},$$
$$\tilde{S} = 0,$$

where $\tau = r/r_c$ and $r^2 = (x - x_c)^2 + (y - y_c)^2$. Here ε represents the strength of the vortex, α controls the decay rate of the vortex, and r_c is the critical radius for which the vortex has the maximum strength. In this paper, we choose $\varepsilon = 0.3, r_c = 0.05$ and $\alpha = 0.204$. The above defined vortex is a steady state solution to the 2-D Euler equation.

We use a grid of 251×101 which is uniform both in the x and y direction. The upper and lower boundaries are set to be reflective. In Figs. 16(a)–(e), we compare the results obtained by WENO-3, MPWENO-5,

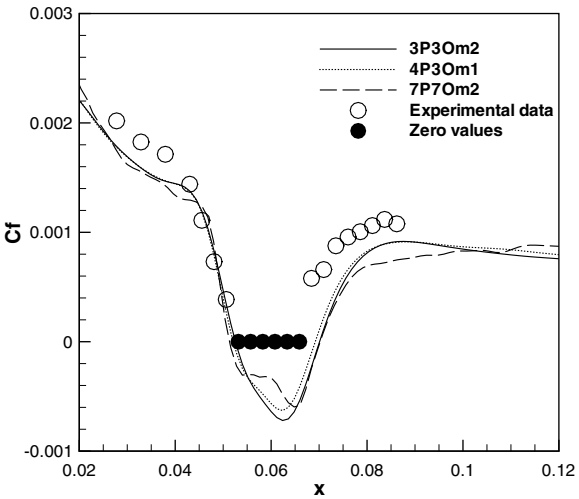

Fig. 15. Coefficient of friction for the shock/boundary-layer interaction.

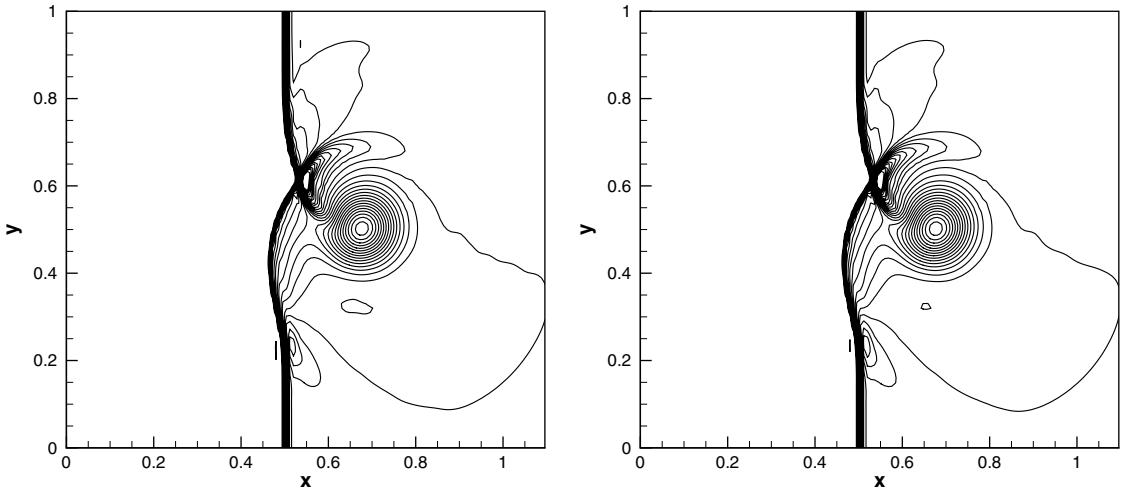
y
x
0
0.2
0.4
0.6
0.8
1

4P3Om1, 3P3Om2 and 7P7Om2. Thirty contours are drawn for the pressure component in the range of (1.02, 1.4). We see that the five schemes give essentially the same resolution, which means our hybrid method for shock-capturing functions quite well. A careful examination reveals that the WENO-3, 4P3Om1 and 3P3Om2 schemes are slightly better in the sense that less numerical noise is generated, which is due to their dissipation properties. And the shock wave captured by 7P7Om2 is the most slender one. This superiority of the 7P7Om2 case is achieved in three ways. First, the MPWENO-5 scheme has a higher formal order; it is at least fifth order. It can resolve sharper shocks on its own than other schemes with lower orders. Second, 7P7Om2 is much less dissipative than the MPWENO-5 scheme. Third, the hybrid between these two schemes is quite effective.

Figs. 17(a)–(e) represent 30 equally spaced pressure contours at $t = 0.8$ with the entire pressure range being $1.1 \leqslant p \leqslant 1.3$. It can be seen that one branch of the shock bifurcations has reached the top boundary and has

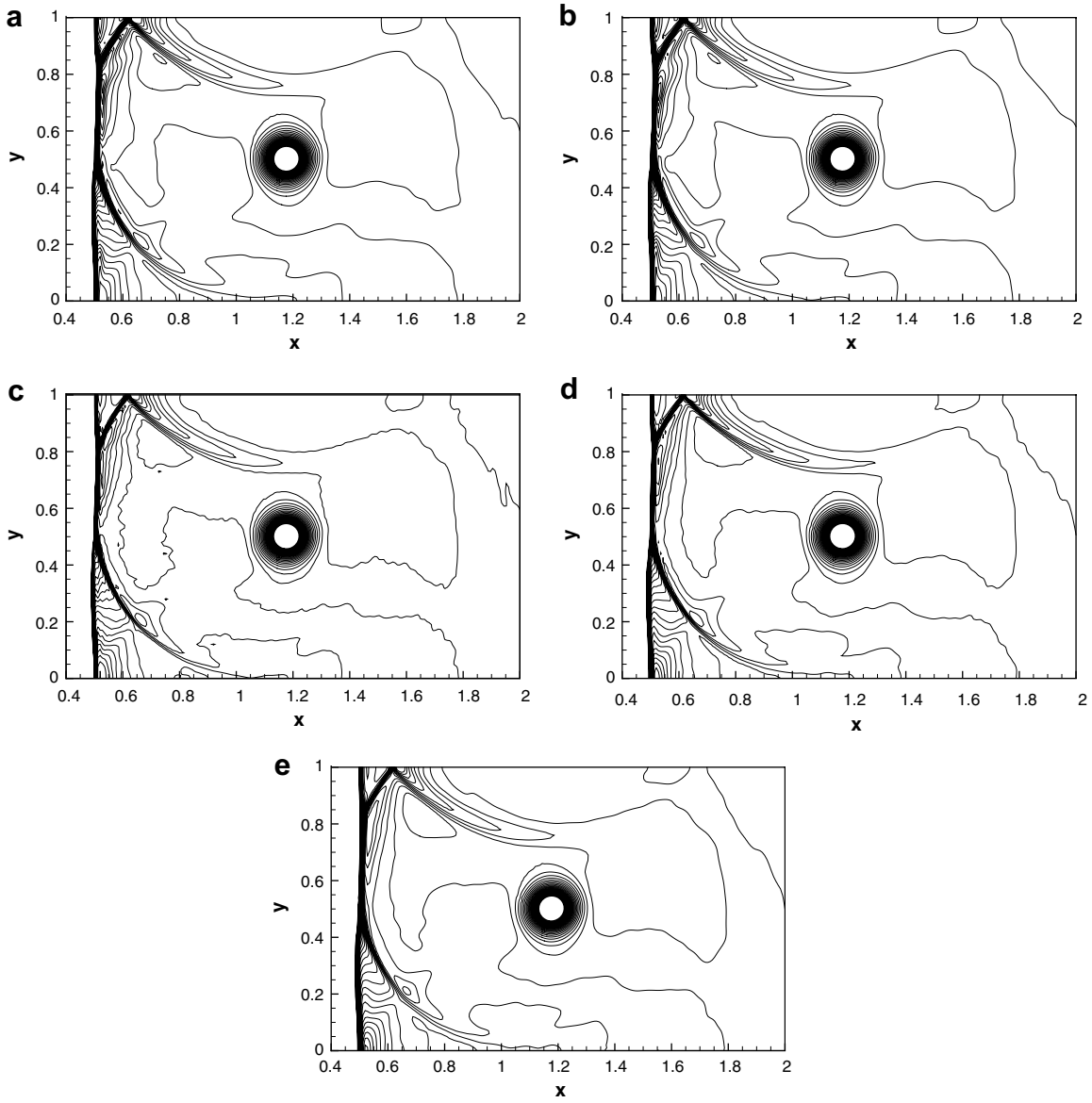

Fig. 17. 2-D shock–vortex interaction. Pressure, Thirty contours from 1.1 to 1.3, $t = 0.8$: (a) 4P3Om1; (b) 3P3Om2; (c) 7P7Om2; (d) MPWENO-5; (e) WENO-3.

been reflected. The reflection is well captured by all these schemes, which indicates that not only the hybrid method but also the boundary closures for the proposed scheme perform well. The shock wave resolved by 7P7Om2 is still the most slender one. Also we can see that the results of the 4P3Om1 and 3P3Om2 schemes are a bit sharper than that of the WENO-3 scheme (see the distributions of contours near shock waves; those of 4P3Om1 and 3P3Om2 are a bit closer to those of MPWENO-5 and 7P7Om2 than those of WENO-3), which may be attributed to the relatively better spectral presentation. (Remember that WENO-3 has a formal order equal to or higher than those of 4P3Om1 and 3P3Om2.)

For our hybrid schemes, the percentage of interfaces on which the WENO fluxes are needed is around 5% during the simulation. When comparing these schemes in terms of computational cost, we find that 4P3Om1 is the fastest one. The CPU time needed to execute one time step for the 4P3Om1 scheme is about 0.24 s, and for 3P3Om2, 7P7Om2, WENO-3 and MPWENO-5, it is 0.26 s, 0.29 s, 0.36 s and 0.56 s on the same machine respectively.

6.4. Decaying compressible isotropic turbulence

Due to the high spectral presentation, the proposed 7P7Om2 scheme has been shown to be very promising for turbulence research. In this section, it is tested by the numerical simulation of decaying compressible isotropic turbulence with an initial Taylor microscale Reynolds number of 72. Based on the Steger–Warming [55] flux vector splitting, the convection terms are discretized by the hybrid version of 7P7Om2. The eighth-order explicit central difference scheme is used to discretize viscous terms, and the three-stage TVD-type Runge–Kutta method is used for time advancement. The simulations are conducted with 128^3 grid points. Then, they are compared with a 128^3 simulation with the spectral-like tenth-order compact finite differencing scheme by Samtaney et al. [68]. The simulations begin with the same initial field, the $D8$ case in Ref. [68], in which the initial turbulent number Mt is 0.5.

In Fig. 18, it can be seen that the present results by using the hybrid scheme agree well with the results of Ref. [68]. This means that the upwind compact 7P7Om2 scheme is not over-dissipative compared with the commonly used non-dissipative Pade schemes and therefore is suitable for turbulence research. The velocity derivative skewness is a high-order statistic, and depends mostly on the high wavenumbers. The fairly good agreement of this quantity verified our results.

However, close observations reveals that the present curve of the normalized turbulent kinetic energy is a bit lower at the early stage. To search for a reasonable explanation for this minor offset, we executed another test for the same case, in which 7P7Om2 was used with no hybridization with MPWENO-5. The results of this

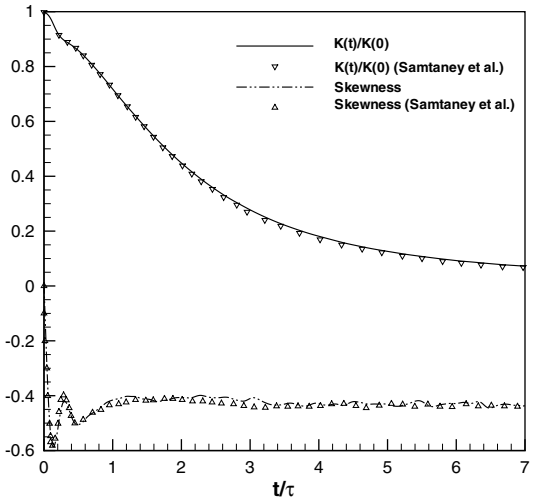

Fig. 19. Normalized turbulent kinetic energy and skewness factor of velocity derivative ($Mt = 0.5$). Only 7P7Om2 is used for convective terms in the simulation.

test are shown in Fig. 19, from which we can see that our results coincide exactly with those from Ref. [68]. Remember that Samtaney et al.'s [68] attempts at DNS of decaying compressible turbulence suffered from a start-up problem; the highest Mt value their simulation could reach was 0.5. They thought the start-up problem was probably related to the appearance of shocklets with associated flow gradients larger than their uniform Pade scheme could resolve. We agree with Samtaney et al.'s [68] explanation. After shocklets develop from the initial field, compact schemes, including the tenth-order Pade scheme and our 7P7Om2 scheme, can introduce strong Gibbs' phenomena in the flow. The Gibbs' phenomena can incur negative pressures or temperatures and finally make the simulations collapse. In the $Mt = 0.5$ case, the highest Mt value the tenth-order Pade scheme can manage, there probably exist Gibbs' phenomena, though they are not strong enough to develop negative pressures or temperatures. Gibbs' phenomena near the shocklets can make the amplitude of velocity fluctuations a bit bigger and therefore the turbulent kinetic energy appears to be a bit higher than the real situation. So, the result from the hybrid version of the 7P7Om2 scheme can be more reasonable. It is expected that our hybrid scheme will lift the maximum initial turbulent Mach number to a higher value. This possibility requires future investigation.

7. Concluding remarks

A family of high-order compact upwind difference schemes has been developed. Due to their combination of the first or both the first and second derivatives, the proposed schemes are more accurate than normal compact difference schemes in the spectral plane. Because all the derivative terms in the schemes appear only on the upwind side of the stencil, the first derivatives can be obtained by efficient methods regardless of whether the boundary is periodic or non-periodic. A new method with the assistant scheme for boundary closure is proposed. The method makes the combinations of boundary schemes and interior schemes FS-stable and therefore can be a general method for boundary closures. Also, based on Ren et al.'s [39] method, an improved efficient shock-capturing method has been developed with good shock-capturing property and higher spectral resolution in the full computational domain, because the application of the WENO schemes is confined only on the points and their near-neighbor points where discontinuity exists.

When our schemes are hybridized with corresponding WENO schemes, from Fourier analysis and computational cost, it can be seen that the 4P3Om1 scheme has the overwhelming advantage of speed, especially when the flow is smooth, in which case no hybridization is needed and therefore the computational cost is only 1/5 and 1/3 of that of the 7P7Om2 scheme with periodic and non-periodic boundary conditions respectively; the 3P3Om2 scheme possesses a bit higher spectral resolution than the 4P3Om1 scheme and it is the most robust one because of its larger dissipation; the 7P7Om2 scheme, though a little more time-consuming than

the 4P3Om1 and 3P3Om2 schemes, is the most accurate one in the spectral plane among all known compact schemes. The good spectral resolution, combined with the almost non-dissipation property at small and moderate wavenumbers and the abundance of dissipation at high wavenumbers, makes it an extremely attractive DNS candidate. At last, both the effectiveness of the new hybrid method and the accuracy of the proposed schemes were verified by executing four benchmark test cases.

The presented schemes can be easily extended by including third or even higher derivatives in them, which may enhance the spectral accuracy of the first derivative to a higher level. However, obtaining the first derivatives from these schemes may be too time-consuming, especially when periodic boundary conditions are adopted. This is why our consideration has been confined to only the first or both the first and second derivatives in the present paper.

Acknowledgments

The authors thank the referees for their encouraging reports and useful comments, which improved the paper significantly. The authors are grateful for the support of the National Natural Science Foundation of China (Nos. 90305014 and 10572074).

Appendix A

The 4P3Om1 scheme:

$$h(a_{1,-1}F_{j-1} + a_{1,0}F_j) = \sum_{n=-1}^{2} a_{0,n}u_{j+n}.$$

Values of coefficients in the 4P3Om1 scheme are listed as follows:

$$a_{1,-1} = 0.4638439991784135\text{E}{+}00, \quad a_{1,0} = 0.1000000000000000\text{E}{+}01,$$
$$a_{0,-1} = -0.1183713998493758\text{E}{+}01, \quad a_{0,0} = 0.8915319975352406\text{E}{+}00,$$
$$a_{0,1} = 0.3042340012323797\text{E}{+}00, \quad a_{0,2} = -0.1205200027386216\text{E}{-}01.$$

The 3P3Om2 scheme:

$$h(a_{1,-1}F_{j-1} + a_{1,0}F_j) + h^2(a_{2,-1}S_{j-1} + a_{2,0}S_j) = \sum_{n=-1}^{1} a_{0,n}u_{j+n},$$
$$h(\bar{a}_{1,-1}F_{j-1} + \bar{a}_{1,0}F_j) + h^2(\bar{a}_{2,-1}S_{j-1} + \bar{a}_{2,0}S_j) = \sum_{n=-1}^{1} \bar{a}_{0,n}u_{j+n}.$$

Values of coefficients in the 3P3Om2 scheme are listed as follows:

$$a_{2,-1} = -0.2415794482633768\text{E}{-}01, \quad a_{2,0} = 0.0000000000000000\text{E}{+}00,$$
$$a_{1,-1} = 0.4275261655209870\text{E}{+}00, \quad a_{1,0} = 0.1000000000000000\text{E}{+}01,$$
$$a_{0,-1} = -0.1165447193107818\text{E}{+}01, \quad a_{0,0} = 0.9033682206946493\text{E}{+}00,$$
$$a_{0,1} = 0.2620789724131689\text{E}{+}00,$$
$$\bar{a}_{2,-1} = -0.8659286486676146\text{E}{-}01, \quad \bar{a}_{2,0} = 0.3268142702664771\text{E}{+}00,$$
$$\bar{a}_{1,-1} = 0.2402214053997156\text{E}{+}00, \quad \bar{a}_{1,0} = 0.1000000000000000\text{E}{+}01,$$
$$\bar{a}_{0,-1} = -0.6201107026998578\text{E}{+}00, \quad \bar{a}_{0,0} = 0.0000000000000000\text{E}{+}00,$$
$$\bar{a}_{0,1} = 0.6201107026998578\text{E}{+}00.$$

The 3P3Om2 scheme:

$$h(a_{1,-1}F_{j-1} + a_{1,0}F_j) + h^2(a_{2,-1}S_{j-1} + a_{2,0}S_j) = \sum_{n=-1}^{1} a_{0,n}u_{j+n},$$

$$h(\bar{a}_{1,-1}F_{j-1} + \bar{a}_{1,0}F_j) + h^2(\bar{a}_{2,-1}S_{j-1} + \bar{a}_{2,0}S_j) = \sum_{n=-1}^{1} \bar{a}_{0,n}u_{j+n}.$$

Values of coefficients in the 7P7Om2 scheme are listed as follows:

$a_{2,-1} = 0.9310913049103751\text{E}-01$, $a_{2,0} = 0.0000000000000000\text{E}+00$,
$a_{1,-1} = 0.6229014060727505\text{E}+00$, $a_{1,0} = 0.1000000000000000\text{E}+01$,
$a_{0,-1} = -0.1272749478440892\text{E}+01$, $a_{0,0} = 0.8339762325591169\text{E}+00$,
$a_{0,1} = 0.5516815213172187\text{E}+00$, $a_{0,2} = -0.1417371978176110\text{E}+00$,
$a_{0,3} = 0.3375371366263799\text{E}-01$, $a_{0,4} = -0.5307617364301992\text{E}-02$,
$a_{0,5} = 0.3828260838312490\text{E}-03$,
$\bar{a}_{2,-1} = 0.1974979614451061\text{E}+00$, $\bar{a}_{2,0} = 0.6167415381304258\text{E}+00$,
$\bar{a}_{1,-1} = 0.8705783531030047\text{E}+00$, $\bar{a}_{1,0} = 0.1000000000000000\text{E}+01$,
$\bar{a}_{0,-1} = -0.9392395461173919\text{E}+00$, $\bar{a}_{0,0} = 0.0000000000000000\text{E}+00$,
$\bar{a}_{0,1} = 0.8737605449787167\text{E}+00$, $\bar{a}_{0,2} = 0.1737383472431471\text{E}+00$,
$\bar{a}_{0,3} = -0.1491265623318568\text{E}+00$, $\bar{a}_{0,4} = 0.4685482662075237\text{E}-01$,
$\bar{a}_{0,5} = -0.5987610393367404\text{E}-02$.

Note that h is set to 1 in the expressions of the 3P3Om2 and 7P7Om2 schemes when optimizations are executed (see Section 2.1 for details), so all simulations using these two schemes must be handled on the computational domain with grid space 1. The metrics of the mapping may then be used to attain the derivatives on the physical grid.

Appendix B

In the following, the boundary closure for the 7P7Om2 scheme is expressed.

For the near-boundary point, the following assistant schemes are suggested

$$u_2' = (c_{2,1}u_1 + c_{2,2}u_2 + c_{2,3}u_3 + c_{2,4}u_4 + c_{2,5}u_5 + c_{2,6}u_6)/h \tag{A2.1a}$$

$$u_2'' = (s_{2,1}u_1 + s_{2,2}u_2 + s_{2,3}u_3 + s_{2,4}u_4 + s_{2,5}u_5 + s_{2,6}u_6 + s_{2,7}u_7)/h^2 \tag{A2.1b}$$

where

$c_{2,1} = 4b + a - 1/3$, $c_{2,2} = -15b - 4a - 1/2$
$c_{2,3} = 20b + 6a + 1$, $c_{2,4} = -10b - 4a - 1/6$
$c_{2,5} = a$, $c_{2,6} = b$
$s_{2,1} = -g - 5q + 11/12$, $s_{2,2} = 5g + 24q - 5/3$
$s_{2,3} = -10g - 45q + 1/2$, $s_{2,4} = 10g + 40q + 1/3$
$s_{2,5} = -5g - 15q - 1/12$, $s_{2,6} = g$, $s_{2,7} = q$.

Substitute Eqs. (A2.1a) and (A2.1b) into the 7P7Om2 schemes (2.12), and let $j = 3$; then we get the scheme on the 3rd point with a, b, g and q as free parameters. Using the procedure listed above we can get the scheme with the optimal resolution satisfying the constraints of stability. The optimized parameters are listed in Table 6 for points $j = 3$ and $j = 4$.

For points $j > 5$, it is hard to find the appropriate combination of these four parameters to yield stable schemes, so we apply the obtained scheme for point $j = 4$ on several points $j \geqslant 5$. In order to apply boundary schemes on fewer points, we propose another group of assistant schemes on point $j = 5$:

Table 6
Optimized parameters for boundary closures for the 7P7Om2 scheme

	top	*a*	*b*	*g*	*q*
$j = 3$	0.5	−0.4597194851313051E−04	−0.2229215518065442E−01	−0.3281278903290147E−02	−0.1903040656679567E−01
$j = 4$	0.5	0.6445072034704367E−02	0.2556920319768490E−01	−0.1133605612534359E−02	−0.6822714905771861E−02
$j = 11$	1.0	−0.5873973995736736E−04	−0.5148455592181436E−03	−0.1041938950948995E−04	−0.9132531330896965E−04

$$u'_5 = (c_{5,1}u_1 + c_{5,2}u_2 + c_{5,3}u_3 + c_{5,4}u_4 + c_{5,5}u_5 + c_{5,6}u_6 + c_{5,7}u_7 + c_{5,8}u_8 + c_{5,9}u_9 + c_{5,10}u_{10})/h, \tag{A2.2a}$$

$$u''_5 = (s_{5,1}u_1 + s_{5,2}u_2 + s_{5,3}u_3 + s_{5,4}u_4 + s_{5,5}u_5 + s_{5,6}u_6 + s_{5,7}u_7 + s_{5,8}u_8 + s_{5,9}u_9 + s_{5,10}u_{10})/h^2, \tag{A2.2b}$$

where

$$\begin{aligned}
&c_{5,1} = 1/140 + a + 8b, \quad c_{5,2} = -1/15 - 8a - 63b\\
&c_{5,3} = 3/10 + 28a + 216b, \quad c_{5,4} = -1 - 56a - 420b\\
&c_{5,5} = 1/4 + 70a + 504b, \quad c_{5,6} = 3/5 - 56a - 378b\\
&c_{5,7} = -1/10 + 28a + 168b, \quad c_{5,8} = 1/105 - 8a - 36b\\
&c_{5,9} = a, \quad c_{5,10} = b\\
&s_{5,1} = g + 8q, \quad s_{5,2} = -8g - 63q + 1/90\\
&s_{5,3} = 28g + 216q - 3/20, \quad s_{5,4} = -56g - 420q + 3/2\\
&s_{5,5} = 70g + 504q - 49/18, \quad s_{5,6} = 3/2 - 56g - 378q\\
&s_{5,7} = -3/20 + 28g + 168q, \quad s_{5,8} = 1/90 - 8g - 36q\\
&s_{5,9} = g, \quad s_{2,10} = q.
\end{aligned}$$

Then optimizations are executed on points $j \geqslant 6$. The schemes are not stable until $j = 11$, and the optimal values of these free parameters for high resolution are also listed in Table 6. For the right boundary schemes, the following expressions are suggested:

$$\begin{aligned}
u'_{N-4} &= \left(\frac{1}{105}u_{N-1} - \frac{1}{10}u_{N-2} + \frac{3}{5}u_{N-3} + \frac{1}{4}u_{N-4} - u_{N-5} + \frac{3}{10}u_{N-6} - \frac{1}{15}u_{N-7} + \frac{1}{140}u_{N-8}\right)\Big/h,\\
u'_{N-3} &= \left(\frac{1}{105}u_{N} - \frac{1}{10}u_{N-1} + \frac{3}{5}u_{N-2} + \frac{1}{4}u_{N-3} - u_{N-4} + \frac{3}{10}u_{N-5} - \frac{1}{15}u_{N-6} + \frac{1}{140}u_{N-7}\right)\Big/h,\\
u'_{N-2} &= \left(-\frac{1}{20}u_{N} + \frac{1}{2}u_{N-1} + \frac{1}{3}u_{N-2} - u_{N-3} + \frac{1}{4}u_{N-4} - \frac{1}{30}u_{N-5}\right)\Big/h,\\
u'_{N-1} &= (2u_N + 3u_{N-1} - 6u_{N-2} + u_{N-3})/6h,\\
u'_{N} &= (3u_N - 4u_{N-1} + u_{N-2})/2h.
\end{aligned} \tag{A2.3}$$

Finally, we list the schemes in the full domain when 7P7Om2 is applied as the interior scheme. The expressions for points $j = 1, 2$ are as follows:

$$\begin{aligned}
u'_1 &= (-3u_1 + 4u_2 - u_3)/6h,\\
u'_2 &= (-u_1 + u_3)/2h.
\end{aligned}$$

For points $j = 3, 4$ the schemes that come from the assistant scheme on the 2nd point are used. The derived schemes on the 4th point are also applied to points $j = 5$ to $j = 10$. For points $j = 11$ the schemes that come from the assistant scheme on the 5th point are used. On points $12 \leqslant j \leqslant N - 5$ the 7P7Om2 schemes are adopted. For points $N - 4 \leqslant j \leqslant N$, the schemes in (A2.3) are used.

References

[1] Jorn Sesterhenn, A characteristic-type formulation of the Navier–Stokes equations for high order upwind schemes, Comput. Fluids 30 (2001) 37–67.

[2] A.I. Tolstykh, Dokl. Akad. Nauk SSSR 210 (1973) 48.
[3] A.I. Tolstykh, in: O.M. Belotserkovskii, V.P. Shidlovsky (Eds.), Current Problems in Computational Fluid Dynamics, MIR, Moscow, 1975.
[4] E.M. Murman, J. Cole, Calculation of plane, steady, transonic flows, AIAA J. 9 (1971) 114–121.
[5] A.I. Tolstykh, Sov. Math. Dokl. 44 (1992) 69.
[6] A.I. Tolstykh, On multioperators principle for constructing arbitrary-order difference schemes, Appl. Numer. Math. 46 (2003) 411–423.
[7] A.I. Tolstykh, Centered prescribed-order approximations with structured grids and resulting finite-volume schemes, Appl. Numer. Math. 49 (2004) 431–440.
[8] Z. Haras, S. Taasan, J. Comput. Phys. 114 (1994) 265.
[9] B. Cockburn, C.-W. Shu, SIAM J. Numer. Anal. 31 (1994) 607.
[10] F. Dexun, M. Yanwen, L. Hong, Upwind compact schemes and applications, in Proceedings, 5th Symp. on Comput. Fluid Dyn., vol. 1, Japan Soc. of Comput. Fluid Dyn., 1993.
[11] M.Y. Shen, Z.B. Zhang, X.L. Niu, A new way for constructing high accuracy shock-capturing generalized compact difference schemes, Comput. Methods Appl. Mech. Eng. 192 (2003) 2703.
[12] S.K. Lele, Compact finite difference schemes with spectral-like resolution, J. Comput. Phys. 103 (1992) 16.
[13] E. Weinan, J.G. Liu, Essentially compact schemes for unsteady viscous incompressible flows, J. Comput. Phys. 126 (1996) 122.
[14] H.L. Meitz, H.F. Fasel, A compact-difference scheme for the Navier–Stokes equations in vorticity–velocity formulation, J. Comput. Phys. 157 (2000) 371.
[15] K. Bhaganagar, D. Rempfer, J. Lumley, Direct numerical simulation of spatial transition to turbulence using fourth-order vertical velocity second-order vertical vorticity formulation, J. Comput. Phys. 180 (2002) 200.
[16] C. Lee, Y. Seo, A new compact spectral scheme for turbulence simulations, J. Comput. Phys. 183 (2002) 438.
[17] S. Nagarajan, S.K. Lele, J.H. Ferziger, A robust high order compact method for large eddy simulation, J. Comput. Phys. 191 (2003) 392.
[18] N. Park, Jung Yul Yoo, Haecheon Choi, Discretization errors in large eddy simulation: on the suitability of centered and upwind biased compact difference schemes, J. Comput. Phys. 198 (2004) 580.
[19] X. Zhong, High-order finite-difference schemes for numerical simulation of hypersonic boundary-layer transition, J. Comput. Phys. 144 (1998) 662.
[20] K.S. Ravichandran, Higher order KFVS algorithms using upwind difference operators, J. Comput. Phys. 130 (1997) 161.
[21] J.A. Ekaterinaris, Implicit, high-resolution compact schemes for gas dynamics and aeroacoustics, J. Comput. Phys. 156 (1999) 272.
[22] A. Lerat, C. Corre, A residual-based compact scheme for the compressible Navier–Stokes equations, J. Comput. Phys. 170 (2001) 642.
[23] R. Hixon, E. Turkel, Compact implicit MacCormack-type schemes with high accuracy, J. Comput. Phys. 158 (2000) 51–70.
[24] F.Q. Hu, M.Y. Hussaini, J.L. Manthey, Low-dissipation and low-dispersion Runge–Kutta schemes for computational acoustics, J. Comput. Phys. 124 (1996) 177.
[25] C.K.W. Tam, J.C. Webb, Dispersion-relation-preserving finite difference schemes for computational acoustics, J. Comput. Phys. 107 (1993) 262.
[26] M.R. Visbal, D.V. Gaitonde, Very high-order spatially implicit schemes for computational acoustics on curvilinear meshes, J. Comput. Acoust. 9 (2001) 1259.
[27] C. Cheong, S. Lee, Grid-optimized dispersion-relation-preserving schemes on general geometries for computational aeroacoustics, J. Comput. Phys. 174 (2001) 248.
[28] Dong-o Jeon, Compact finite difference method for calculating magnetic field components of cyclotrons, J. Comput. Phys. 132 (1997) 167.
[29] J.S. Shang, High-order compact-difference schemes for time-dependent Maxwell equations, J. Comput. Phys. 153 (1999) 312.
[30] J.S. Shang, Solving schemes for computational magneto-aerodynamics, J. Sci. Comput. 25 (1) (2005) 289.
[31] L. Ge, J. Zhang, High accuracy solution of convection diffusion equation with boundary layers on nonuniform grids, J. Comput. Phys. 171 (2001) 560.
[32] M.-C. Lai, A simple compact fourth-order Poisson solver on polar geometry, J. Comput. Phys. 182 (2002) 337.
[33] T. Nihei, K. Ishii, A fast solver of the shallow water equations on a sphere using a combined compact difference scheme, J. Comput. Phys. 187 (2003) 639.
[34] M.A. Tolstykh, Vorticity-divergence semi-Lagrangian shallow-water model of the sphere based on compact finite differences, J. Comput. Phys. 179 (2002) 180.
[35] J. Zhang, Multigrid method and fourth-order compact scheme for 2D Poisson equation with unequal mesh-size discretization, J. Comput. Phys. 179 (2002) 170.
[36] T.K. Sengupta, G. Ganeriwal, S. De, Analysis of central and upwind compact schemes, J. Comput. Phys. 192 (2003) 677.
[37] K. Mahesh, A family of high order finite difference schemes with good spectral resolution, J. Comput. Phys. 145 (1998) 332.
[38] B. Gustafsson, H.O. Kreiss, A. Sundström, Stability theory of difference approximations for mixed initial boundary value problems. II, Math. Comput. 26 (1972) 649.
[39] Yu-Xin Ren, Miao'er Liu, Hanxin Zhang, A characteristic-wise hybrid compact-WENO scheme for hyperbolic conservation laws, J. Comput. Phys. 192 (2003) 365.
[40] N.A. Adams, K. Shariff, A high-resolution hybrid compact-ENO scheme for shock-turbulence interaction problems, J. Comput. Phys. 127 (1996) 27.

[41] Dinshaw S. Balsara, Chi-Wang Shu, Monotonicity preserving weighted essentially non-oscillatory schemes with increasingly high order of accuracy, J. Comput. Phys. 160 (2000) 405–452.
[42] X.D. Liu, S. Osher, T. Chan, Weighted essentially nonoscillatory schemes, J. Comput. Phys. 115 (1994) 200.
[43] Mahmood K. Mawlood, ShahNor Basri, Waqar Asrar, Ashraf A. Omar, Ahmad S. Mokhtar, Megat M.H.M. Ahmad, An AUSM-based high-order compact method for solving Navier–Stokes equations, Aircr. Eng. Aerosp. Technol. 76 (2004) 299.
[44] K.M. Oliger, J.D. Mo, M.A. Driver, Shock wave/flat plate boundary layer/injection interactions, AIAA paper. AIAA-95-2481, 1995.
[45] S. Pirozzoli, Conservative hybrid compact-WENO schemes for shock–turbulence interaction, J. Comput. Phys. 178 (2002) 81.
[46] A. Jameson, W. Schmidt, E. Turkel, Numerical Solutions of the Euler Equations by Finite Volume Methods Using Runge–Kutta Time-Stepping Schemes. AIAA Paper. AIAA-81-1259, 1981.
[47] T.K. Sengupta, Fundamentals of Computational Fluid Dynamics, University Press, Hyderabad, India, 2004.
[48] T.K. Sengupta, S.K. Sircar, A. Dipankar, High accuracy schemes for DNS and acoustics, J. Sci. Comput. 26 (2) (2006) 151.
[49] T.K. Sengupta, A. Dipankar, A comparative study of time advancement methods for solving Navier–Stokes equations, J. Sci. Comput. 21 (1) (2004) 225.
[50] T.K. Sengupta, G. Ganeriwal, A. Dipankar, High accuracy compact schemes and Gibbs' phenomenon, J. Sci. Comput. 21 (3) (2004) 253.
[51] A. Dipankar, T.K. Sengupta, Symmetrized compact scheme for receptivity study of 2D transitional channel flow, J. Comput. Phys. 215 (2006) 245.
[52] T.K. Sengupta, A. Guntaka, S. Dey, Navier–Stokes solution by new compact scheme for incompressible flows, J. Sci. Comput. 21 (3) (2004) 269.
[53] G.S. Jiang, C.W. Shu, Efficient implementation of weighted ENO schemes, J. Comput. Phys. 126 (1996) 202.
[54] C.W. Shu, S. Osher, Efficient implementation of essentially non-oscillatory shock-capturing schemes II, J. Comput. Phys. 83 (1989) 32.
[55] J.L. Steger, R.F. Warming, Flux vector splitting of the inviscid gasdynamic equations with application to finite difference methods, J. Comput. Phys. 40 (1981) 263.
[56] C.D. Pruett, T. Zang, C.-L. Chang, M.H. Carpenter, Theor. Comput. Fluid Dyn. 7 (1995) 49.
[57] Jichun Li, Miguel R. Visbal, High-order compact schemes for nonlinear dispersive waves, J. Sci. Comput. 26 (1) (2006) 1–23.
[58] R. Vichnevetsky, J.B. Bowles, Fourier analysis of numerical approximations of hyperbolic equations, SIAM, Philadelphia, 1982.
[59] K. Schittkowski, Annu. Oper. Res. 5 (1985) 485.
[60] J. Stoer, Principles of sequential quadratic programming methods for solving nonlinear problems, in: K. Schittkowski (Ed.), Computational Mathematical Programming, NATO ASI Series F, vol. 15, Springer-Verlag, Berlin, 1985, p. 165.
[61] A.I. Tolstykh, Compact Difference Schemes and Their Application to Problems of Aerohydrodynamics, Nauka, Moscow, 1990.
[62] V.A. Garanzha, A.I. Tolstykh, On numerical simulation of unsteady incompressible flows on the bases of fifth-order compact approximations, Dokl. Acad. Nauk SSSR 312 (1990) 311 (in Russian).
[63] M.A. Tolstykh, Application of fifth-order compact upwind differencing to moisture transport equation in atmosphere, J. Comput. Phys. 112 (1994) 394.
[64] A.D. Gosman, B.E. Launder, G.J. Reece, Computer-Aided Engineering Heat Transfer and Fluid Flow, John Wiley & Sons, New York, 1985, pp. 55–56.
[65] J.P. Van Doormaal, G.D. Raithby, Enhancements of the simple method for predicting incompressible fluid flow, Numer. Heat Transf. 7 (1984) 147.
[66] S.V. Patankar, C.H. Liu, E.M. Sparrow, Fully developed flow and heat transfer in ducts having streamwise-periodic variations of cross-sectional area, J. Heat Transf. 99 (1977) 180.
[67] R.J. Hakkinen, I. Greber, L. Trilling, S.S. Abarnel, The interaction of an oblique shock wave with laminar boundary layer, Fluid Dynamics Research Group M.I.T., TR (1957) 57–61.
[68] R. Samtaney, D.I. Pullin, B. Kosovic, Direct numerical simulation of decaying compressible turbulence and shocklet statistics, Phys. Fluids 13 (5) (2001) 1415–1430.